batteries

Article

Mechanical Characterization and Modeling of Large-Format Lithium-Ion Battery Cell Electrodes and Separators for Real Operating Scenarios

Johannes Brehm [1,2,*], Axel Durdel [1], Tobias Kussinger [1,2], Philip Kotter [2], Maximilian Altmann [2] and Andreas Jossen [1]

[1] Chair of Electrical Energy Storage Technology (EES), Department of Energy and Process Engineering, TUM School of Engineering and Design, Technical University of Munich (TUM), Arcisstrasse 21, 80333 Munich, Germany
[2] Bayerische Motoren Werke Aktiengesellschaft (BMW AG), Petuelring 130, 80809 Munich, Germany
* Correspondence: johannes.brehm@tum.de

Abstract: This study presents a novel application-oriented approach to the mechanical characterization and subsequent modeling of porous electrodes and separators in lithium-ion cells to gain a better understanding of their real mechanical operating behavior. An experimental study was conducted on the non-linear stiffness of $LiNi_{0.8}Co_{0.15}Al_{0.05}O_2$ and graphite electrodes as well as PE separators, harvested from large-format lithium-ion cells, using compression tests. The mechanical response of the components was determined for different operating conditions, including nominal stress levels, mechanical loading rates, and mechanical cycles. The presented work describes the test procedure, the experimental setup, and an objective evaluation method, allowing for a detailed summary of the observed mechanical behavior. A distinct nominal stress level and mechanical cycle dependency of the non-linear stiffnesses of the porous materials were found. However, no clear dependency on compression rate was observed. Based on the experimental data, a poroelastic mechanical model was utilized to predict the non-linear behavior of these porous materials under real mechanical operating scenarios with a normalized root-mean-squared error less than 5.5%. The results provide essential new insights into the mechanical behavior of porous electrodes and separators in lithium-ion cells under real operating conditions, enabling the accelerated development of high-performing and safe batteries for various applications.

Keywords: lithium-ion battery; operation; NCA; graphite; PE separator; uniaxial mechanical characterization; non-linear modeling

check for updates

Citation: Brehm, J.; Durdel, A.; Kussinger, T.; Kotter, P.; Altmann, M.; Jossen, A. Mechanical Characterization and Modeling of Large-Format Lithium-Ion Battery Cell Electrodes and Separators for Real Operating Scenarios. *Batteries* **2024**, *10*, 422. https://doi.org/10.3390/batteries10120422

Academic Editors: Jie Deng and Chulheung Bae

Received: 1 November 2024
Revised: 25 November 2024
Accepted: 26 November 2024
Published: 29 November 2024

Copyright: © 2024 by the authors. Licensee MDPI, Basel, Switzerland. This article is an open access article distributed under the terms and conditions of the Creative Commons Attribution (CC BY) license (https://creativecommons.org/licenses/by/4.0/).

1. Introduction

The increasing demand for high-performing and safe battery systems has motivated research on the mechanical characterization and modeling of large-format lithium-ion cell electrodes and separators. Understanding their mechanical properties is essential for optimizing design and preventing failures like cracking and delamination. Characterizing these materials under different operating conditions allows for the identification of critical parameters such as stiffness and strength [1–11]. Models that build on the findings of these experimental data can provide insights into the impact of mechanical loading on electrochemical performance [1,8,12–17]. Improving characterization and modeling supports the development of safer, more durable batteries, benefiting industries relying on lithium-ion batteries, such as electric vehicles (EVs) and renewable energy storage [4,18–21].

Since 2018, a series of publications have explored the mechanical properties of battery cells and their sub-components (such as jelly rolls, stacks, or isolated electrodes and separators) by applying external mechanical loading, as presented in the literature [1–11]. An overview of the respective experimental design is given in Table 1, with this work added at

the end of the table. Nevertheless, from an EV operation point of view, research in the field of mechanical characterization requires further investigation, as follows:

- Investigations comprise only laboratory-sized or small commercial cells [1–4,10]. Studies of large prismatic cells, commonly used in EV, are missing.
- Stress ranges $\sigma_{min} - \sigma_{max}$ and compression rates v are seldom chosen in relation to real boundary conditions, rendering a transfer from the literature to application difficult [1–11].
- Only one investigation exists that utilizes more than one mechanical cycle n [3].
- Samples are mostly conditioned without electrolytes [1,4–6,9–11] or in a low state of charge (SoC) [1–4,9,11], making direct comparisons to real operations difficult.

Table 1. A literature review of mechanical characterization investigations utilizing compression tests. The column labeled 'Elyt.' indicates whether tests were conducted using dry electrodes or electrodes filled with electrolytes. Literature data in the compression rate v column were converted to MPa h^{-1} for comparability. In case the respective reference utilized a displacement-controlled test procedure, the resulting pressures during the procedure are given here as force-controlled equivalents.

Refs.	Scope	Material	SoC in %	Elyt.	σ_1 in MPa	σ_{nom} (σ_{min}–σ_{max}) in MPa	v in MPa h^{-1}	Cycles n in —	Application/Focus
[1]	layers	NMC_{111}, PE, Gr	0	no	0.30	1.65 (0.30–3.00)	70.74	1	modeling normal operation
[2]	layers pouch	NMC_{622}, NMC_{811}, PE, Gr, Si/Gr	0	yes [b] no [c]	0.06	0.08 [d] 0.42 [d] 0.84 [d]	—	—	compressibility characterization only
[3]	layers pouch	LCO/NCA, PP, Gr	0	yes [a]	0.02	1.00 [d] 1.10 (1.00–1.20) 3.00 [d] 6.00 [d] 10.00 [d]	20.37×10^1	— 3 — — —	effect on local current densities
[4]	layers	NMC_{811}, PE, Gr	0	no	1.00	(1.00–200.00)	37.41×10^2 12.47×10^3	—	crash modeling
[5]	layers	PE, PP	n.d.	no	0.00	(0.00–150.00) (0.00–135.00) (0.00–90.00)	31.32×10^4 36.45×10^3 24.30	1	temperature and strain rate dependency of polymer separator
[6]	layers	PP	n.d.	no	1.00	(1.00–10.00) (1.00–20.00) (1.00–40.00) (1.00–60.00) (1.00–80.00) (1.00–100.00)	11.72×10^4 14.84×10^4 41.55×10^3 11.92×10^3 12.34×10^3 13.65×10^3	1	ion transport of PP separator under compression
[7]	layers	PE, PP	n.d.	yes	0.50	(0.50–80.00)	17.39×10^2 17.02×10^1 16.49 16.00×10^{-1} 15.69×10^{-2} 15.40×10^{-3}	1	temperature-dependent stiffness of PE separators
[8]	layers	PE	n.d.	yes	0.00	(0.00–22.50) (0.00–33.00) (0.00–45.00) (0.00–52.50)	1.22 17.82 24.30×10^1 28.35×10^2	1	hyper-viscoelastic model for battery separators
[9]	layers pouch	NMC_{622}, PE, Gr	0 [b] 0–100 [c]	no [b] yes [c]	0.05	(0.05–1.75)	n.d.	1	measuring reversible swelling

Table 1. *Cont.*

Refs.	Scope	Material	SoC in %	Elyt.	σ_1 in MPa	σ_{nom} (σ_{min}–σ_{max}) in MPa	v in MPa h^{-1}	Cycles n in —	Application/Focus
[10]	layers pouch	NMC_{811}, PP, Si/Gr	0 [b] 0 [c], 70 [c], 100 [c]	no [b] yes [c]	—	1.50 (0.00–3.00)	10.00×10^{-1} [b] 30.24 [d]	1	modeling normal operation
[11]	layers pouch	NMC_{811}, PE, PP, Gr	0 [b] 0–100 [c]	no [b] yes [b,c]	0.20	(0.20–2.50)	n.d.	1	effect of assembly pressure on cell performance
this work	layers	NCA, PE, Gr	0	no	0.08	0.30 (0.10–0.50) 1.00 (0.80–1.20) 3.00 (2.80–3.20)	20.00×10^{-2} 60.00×10^{-2} 10.00×10^{-1}	10	modeling normal operation

[a] replaced by diethyl carbonate, [b] component multi-layer level, [c] pouch cell level, [d] constant pressure.

The main objective of this work is to extend the state of the art by a characterization procedure and modeling approach, which have not been previously addressed regarding the following aspects:

I. Determining the real mechanical operation behavior of the electrodes and separator by conducting cyclic mechanical compression tests to mimic the real mechanical operating scenario of a large-format battery cell. Related research questions are as follows:
   - Is the mechanical behavior dependent on the compression rate v for a given nominal stress σ_{nom}?
   - Is the mechanical behavior dependent on the nominal stress σ_{nom} for a given compression rate v?
   - Is the mechanical behavior dependent on the number of mechanical cycles n?
   - Is the mechanical behavior identical for compression and decompression?

II. Non-linear poroelastic material modeling approach to depict the mechanical behavior of porous electrodes and separators more precisely. The pertinent research question can be stated as follows:
   Can a model be used for fitting over various force levels and compression rates?

Therefore, cyclic mechanical compression tests were conducted with harvested electrodes and separators. The measurement data were subsequently used to investigate the mechanical compression behavior of the single-cell components regarding the evolution of plastic strain over cycling as well as the maximum strain. In the second part of the results section, a modeling approach is presented that enables an accurate representation of cyclic load scenarios.

2. Experimental

2.1. Sample Materials and Preparation

A large-format prismatic 70.2 A h cell underwent formation, was discharged at 0.1 C to 2.8 V, and was disassembled in an argon-filled glovebox (M. Braun Inertgas-Systeme GmbH, Garching, Germany, O_2 and $H_2 < 1$ ppm) at 25 °C [22]. The respective (active) materials are as follows: graphite (Gr) for the anode, nickel-cobalt-aluminum (NCA) for the cathode, and polyethylene (PE) for the separator. Harvested electrode and separator sheets were washed in DEC for 10 min. Subsequently, coin samples at ∅ 18 mm were prepared with a handheld precision punch (Nogamigiken Co., Ltd., Hitachiomiya, Japan) [23]. A schematic showing the electrode sheets and punched samples is given in Figure 1a. The samples were stored inside the glovebox until needed for compression tests as described in Section 2.3.

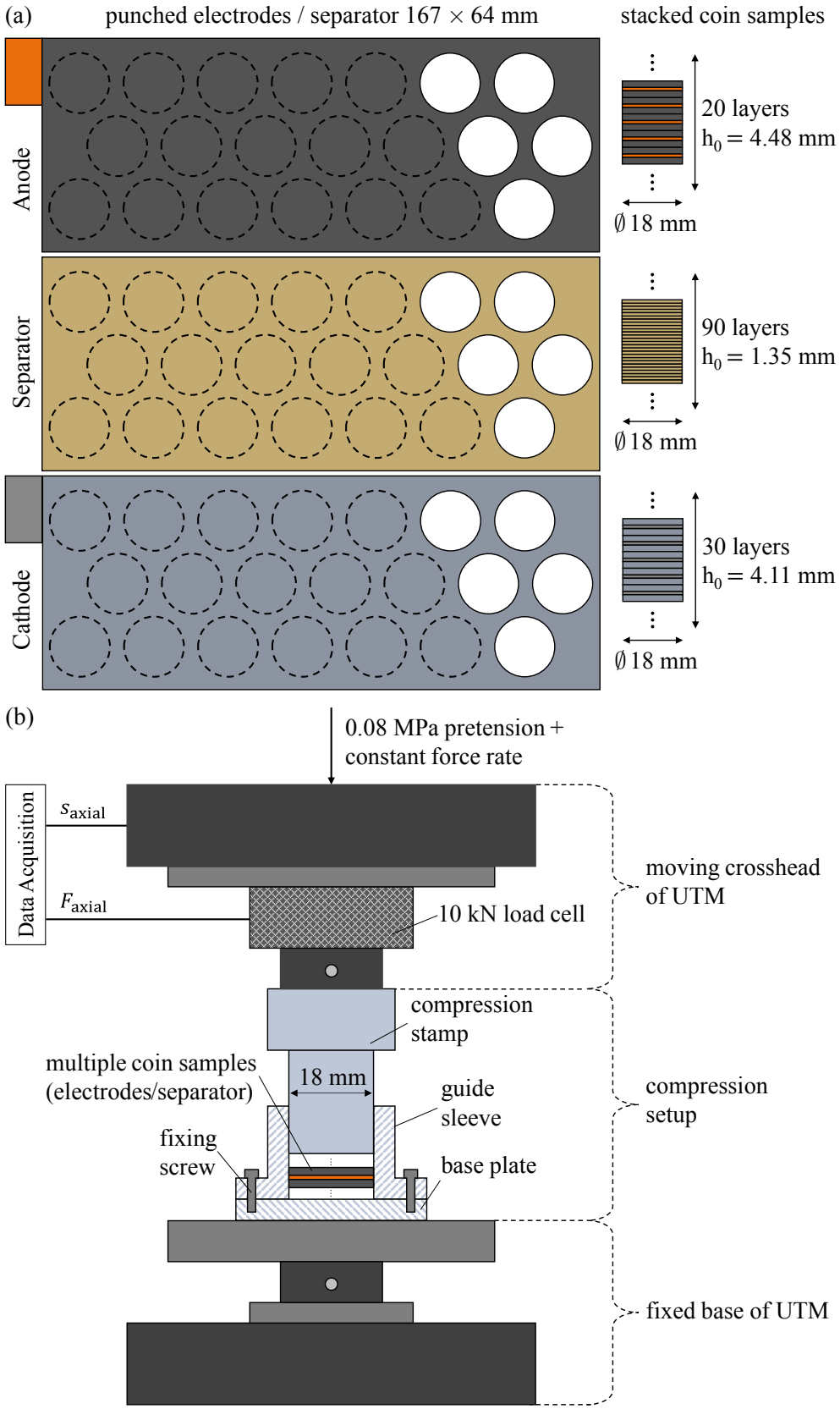

Figure 1. (**a**) Schematic sample preparation for the anode, separator, and cathode. The dashed circles represent coins that are being punched out, and the white circles represent coins that have already been punched out. Punched coin samples are stacked as indicated on the right. (**b**) Schematic overview of the used compression test setup with all sub-components.

2.2. Test Setup

The uniaxial compression tests were carried out using an AllroundLine Z010 universal testing machine (UTM) from ZwickRoell (ZwickRoell GmbH & Co. KG., Ulm, Germany) [24]. The displacement was measured via the UTM spindle drive with an accuracy of ±0.6 nm [24]. The force was recorded with an Xforce P 10 kN load cell (ZwickRoell GmbH & Co. KG., Ulm, Germany), exhibiting a non-linearity of ±0.5% [25].

A custom-built test setup (as shown in Figure 1b, which included a compression stamp and a guide sleeve, was used for the compression tests. The entire setup was made from stainless steel and was intended to prevent any misalignment of the stacked samples prior to (as well as during) the test. The stack of samples was placed inside the guidance sleeve, which was attached to a base plate. The base plate was mounted on the fixed base of the UTM and remained stationary during the compression test. The guidance sleeve's inner diameter was 18.05 mm so that the coin samples tightly fit. The compression stamp with an outer diameter of 18.00 mm was attached to the moving crosshead of the UTM. The compression stamp tightly fitted into the guidance sleeve, applying pressure onto the samples.

Note that the applied force was uniaxial, and due to the test setup including mechanical limitations in the lateral direction, the resulting strain was considered to be uniaxial, too. The test setup without samples was used for reference measurements, which were subsequently utilized for the raw data correction with the stiffness of the machine and setup. This is of great importance due to the significant elastic deformation of the spindle drive of the UTM and/or the test setup itself [3,26–28]. The overall elastic deformation of our entire system without samples was $\leqq 42$ µm in the work areas used.

2.3. Test Protocol

Coin samples were taken from the glovebox and placed inside the guidance sleeve of the compression setup. Multiple samples were stacked (20 anodes, 30 cathodes, or 90 separators) following recommendations from [29]. Additionally, multiple samples increased the total sample thickness and, thus, decreased the signal-to-noise ratio. Subsequently, the test protocol was started. Note that the test was conducted using dry electrodes (no electrolytes) under constant atmospheric conditions at 25 °C, to minimize the influence of these environmental factors.

The test procedure initially applied a pre-load of 20 N (σ_1 = 0.08 MPa) at which the strain was defined to be zero. Preliminary tests have shown that this pre-load is needed so that the individual layers in the sample stack have a well-defined contact. From this point onward, the actual compression test started. A schematic is shown in Figure 2. Starting from stress σ_1, a constant compression rate v was applied until σ_{min} was reached. In the following, $n = 10$ mechanical cycles with the same (de)compression rate v were carried out between σ_{min} and σ_{max}. These cycles were exclusively mechanical in nature and, therefore, do not represent electrochemical cycles and associated effects. The first compression from σ_1 over σ_{min} to σ_{max} was carried out without any interruption. The final decompression of the n-th cycle analogously started at σ_{max} and continued over σ_{min} until the stress reached σ_1 again and the test terminated. Note that the nominal operational stress σ_{nom} was centered between σ_{min} and σ_{max}. The respective stress values σ and compression rates v can be found in Section 2.4. During the tests, the force was applied, while force and displacement were measured as the time series sampled every 0.01 µm and 0.5 min. Since the force was applied to a defined contact area between the compression stamp and the sample, the stress was known. From the displacement and the initial height at pre-load h_1 given in Table 2, the strain was calculated.

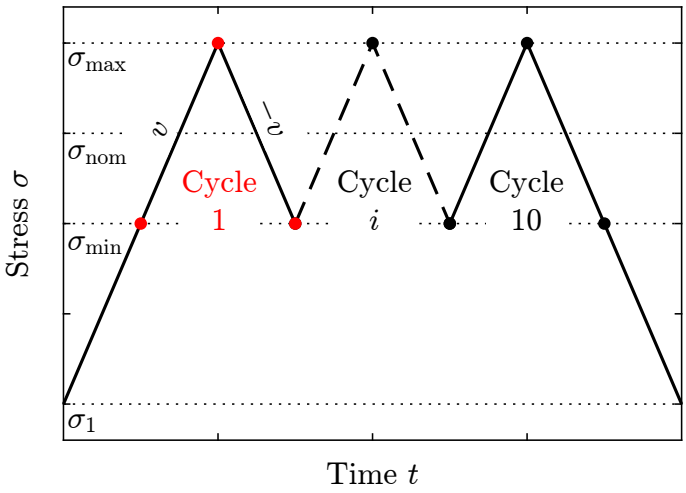

Figure 2. Schematic test program for characterizing the stacked electrode coin samples with all relevant process variables: pre-load stress σ_1, minimum stress σ_{min}, nominal stress σ_{nom}, maximum stress σ_{max}, compression rate v, and cycle count i.

2.4. Design of Experiment

Overall, three different nominal stresses σ_{nom} and three different compression rates v were tested, as shown in the last row of Table 1. The tests were conducted for the anode, separator, and cathode, respectively, resulting in 27 individual tests.

The nominal stresses were derived from the total stack pressure of a battery module with several cells at different points during its lifetime. At begin of life (BoL), the average stack pressure was approx. 0.3 MPa, while at end of life (EoL), it tose approx. up to 3.0 MPa due to aging [30–32]. The third value of 1.0 MPa was chosen between the other two values. Moreover, the three chosen nominal stress levels σ_{nom} enabled the investigation of a possible non-linear mechanical material behavior. Accounting for such non-linear material behavior during characterization might become important, especially for predictions over a lifetime.

Table 2. Measured component characteristics for the Gr anode, PE separator, and NCA cathode used.

	Unit	Gr Anode	PE Separator	NCA Cathode
Content of active material	%$_{wt}$	95.7 [a]	—	95.4 [b]
Content of non-active material	%$_{wt}$	4.3 [c]	—	4.6 [c]
Total layer thickness, stress-free L_0	µm	224 [d]	15 [d]	137 [d]
Thickness current collector L_0	µm	8 [d]	—	11 [d]
Thickness coating, stress-free L_0	µm	108 [d]	—	63 [d]
Porosity coating ϵ_l	–	0.309 [e]	0.519 [e]	0.187 [e]
Initial void-to-solid ratio, stress-free $\epsilon^0_{l/s}$	–	0.447 [f]	1.079 [f]	0.230 [f]
Number of layers	–	20	90	30
Total sample height, no load h_0	mm	4.480 [f]	1.350 [f]	4.110 [f]
Total sample height, pre-load h_1	mm	4.395 [g]	1.304 [g]	4.060 [g]

[a] determined by simultaneous thermal analysis with mass spectroscopy (STA-MS), [b] determined by inductively coupled plasma-optical emission spectrometry (ICP-OES), [c] determined by fourier transform infrared spectroscopy (FT-IR), [d] determined by scanning electron microscopy (SEM) cross-section, [e] determined by helium pycnometer, [f] calculated, [g] UTM.

The operational pressure window between 0% and 100% of the full cell SoC at BoL, as measured by Spingler et al. [3], is approx. 0.3 MPa during electrochemical cycling at 1.0 MPa with initial pressure. Cannarella et al. [15], however, measured an operational window of approx. 0.4 MPa at an initial pressure of 0.05 MPa. In the present study, the initial pressure σ_1 is chosen at 0.08 MPa, which is close to the value reported by Cannarella et al.; thus, the operational window is 0.4 MPa. Aufschläger et al. [33] cycled pouch cells at different mechanical bracing forces. Their results show similar operating windows regardless of the applied pressure, even throughout the cyclic aging. Experimental data from ongoing tests using the same batteries as in this work have shown an increase in the stack pressure of approximately 0.2 MPa, which is within the range given by the literature.

The compression rates are chosen to be equivalent to C-rates of 1C, 3C, and 5C. Examples of large-format cells cycled up to 2C that also provide mechanical data can be found in [3,15,33,34]. Note that 1C means that an increase in pressure by 0.2 MPa — the assumed operational window during electrochemical cycling — is carried out by the UTM within 1 h. This is equal to the loading a large-format Li-ion cell faces during a continuous charge with a rate of 1C. Accordingly, a 1C compression by 0.4 MPa between $\sigma_{\min}$ and $\sigma_{\max}$ during the actual test was carried out in 2 h. Tests at smaller compression rates could not be carried out due to limited continuous access to the UTM but would be of interest in the future to further investigate the rate-dependency of the stress–strain relationship.

3. Modeling

In addition to mechanical characterization, this work investigates material modeling approaches for porous battery sub-components. A material model, or constitutive model, is a mathematical representation of the expected deformation behavior of a given material in response to an applied load [35], and can be written as follows:

$$\boldsymbol{\sigma} = \boldsymbol{C} \cdot \boldsymbol{\varepsilon} \tag{1}$$

where $\boldsymbol{\sigma}$ denotes the stress tensor, $\boldsymbol{C}$ denotes the stiffness tensor, and $\boldsymbol{\varepsilon}$ denotes the 2nd-order strain tensor (for details, see Equation (A1)).

Since the compression tests are uniaxial, Poisson's ratio for our electrodes is unknown, and $\nu = 0$ is assumed, as in [36–39]. This results in no shear forces. As the compression tests in this work were used to derive a description of the elastic behavior of the mechanical properties of the components, any effects due to shear forces were already taken into account implicitly. Since only uniaxial stresses/strains occurred later on, the indices are omitted below, and $\sigma_{11} = \sigma$, resp., $\varepsilon_{11} = \varepsilon$ apply. Note that in theory, the stiffness tensor $\boldsymbol{C}$ as well as Young's modulus E and Poisson ratio ν, may depend on the electrode's degree of lithiation (DoL) and electrolyte content. However, compression tests have only been conducted at a 0% full cell SoC at dry conditions. Thus, mechanical properties depending on lithiation and electrolyte viscoelasticity are not considered in this work. In this work, two model approaches are compared to represent the mechanical behavior of the components, as follows:

(1) *Hooke's Law*, a linear-elastic model, which represents the simplest (but a common) approach (Section 3.1).
(2) *Poroelasticity*, a non-linear-elastic model, which represents a novel approach, considering the porous property of the components (Section 3.2).

Both approaches as well as their evaluation procedures (Section 3.3) will be briefly introduced below.

3.1. Hooke's Law (Linear Elasticity)

Hooke's law is a basic principle in solid mechanics that describes the linear relationship between the applied force and the resulting deformation of an elastic material. First formulated by the English scientist Robert Hooke in the 17th century [40], this fundamental law has been extensively used in the analysis and design of mechanical systems and

structures, e.g., electrode materials of lithium-ion cells [12,41–43]. Considering uniaxial conditions, Hooke's Law can be derived from Equation (1) as follows:

$$\sigma(\varepsilon) = E \cdot \varepsilon \tag{2}$$

3.2. Poroelasticity (Non-Linear Elasticity)

Poroelasticity describes the mechanical non-linear behavior of materials with porous structures; it is commonly used in the fields of civil engineering, materials engineering, geology, hydrogeology, and soil science [44–48]. In the context of lithium-ion battery electrodes and separators, the porous nature of these materials plays a crucial role in their electrochemical performance and their mechanical response. Due to the similarity between the porous morphology of the battery sub-components and soil, the approach used in this work originates from the field of soil modeling [48] and was later recommended/utilized by [49] for modeling poroelastic material behaviors.

The poroelastic model provides a more comprehensive description of the material behavior compared to the traditional linear-elastic approach described by Hooke's law, which does not explicitly consider the porous microstructure property. A detailed derivation can be found in Appendix B.2. Here, only the essential equations are shown for readability. The uniaxial stress σ is defined as follows:

$$\sigma(\varepsilon) = (\sigma_0 + \sigma_t) \cdot \left(2 \cdot \varepsilon \cdot \frac{1 + \epsilon^0_{l/s}}{\kappa} + 1 \right) \cdot \exp\left[\varepsilon \cdot \frac{1 + \epsilon^0_{l/s}}{\kappa} \right] - \sigma_t \tag{3}$$

Here, σ_0 denotes the initial stress, σ_t denotes the elastic tensile strength, κ denotes the logarithmic bulk modulus, and $\epsilon^0_{l/s}$ denotes the initial void-to-solid ratio, defined as follows:

$$\epsilon^0_{l/s} = \frac{V^0_l}{V^0_s} = \frac{\epsilon^0_l}{1 - \epsilon^0_l} \tag{4}$$

The value of $\epsilon^0_{l/s}$ can consequently range from 0 to infinity.

The model parameterization process subsequently aims to determine the optimal values of κ and σ_t to adapt the poroelastic model from Equation (3) to the experimental stress–strain data. The key steps in the model parameterization process are as follows:

(1) Identification of the parameters to be optimized: Logarithmic bulk modulus κ and elastic tensile strength σ_t are selected as the parameters to be optimized, as they are the unknown variables in Equation (3). All other parameters are either measured or known, as shown in Table 2.
(2) Utilization of the MATLAB 2023b Curve Fitting Toolbox: The optimization is performed using the Curve Fitting Toolbox in MATLAB 2023b, employing a nonlinear least squares method with a trust-region algorithm.
(3) Fitting the model to the data: Equation (3) is used as the model, and the optimizer is employed to fit the values of κ and σ_t to the available data.

3.3. Model Evaluation

The following briefly explains how the two modeling approaches are compared with each other and which error metrics are used to determine their goodness. For parameterizing and evaluating the models in this work, only the range between σ_{min} and σ_{max} for the respective nominal stresses σ_{nom} are considered (see Table 1, Figure 2).

3.3.1. Model Comparison Based on Zero-Shifted Data

Since only the range between σ_{min} and σ_{max} is used, the data of the mechanical cycles are shifted to zero, i.e., the starting point of each cycle is shifted to $(\sigma, \varepsilon) = (0, 0)$. This results in a fitting procedure as depicted in Figure 3a.

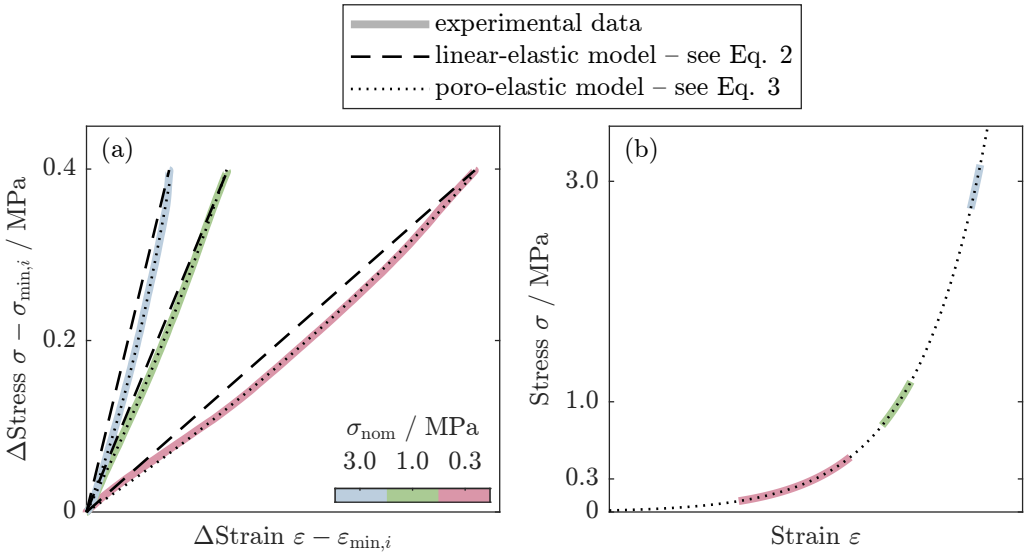

Figure 3. Schematic overview of the two utilized modeling approaches: (**a**) Comparison of the linear-elastic approach vs. poroelastic approach, fitted to the respective cycles set to zero, and (**b**) poroelastic approach fitted to the raw data.

3.3.2. Poroelastic Fit of the Raw Data

In addition to the model comparison based on zero-shifted data, the poroelastic model is also fitted against the raw data without any shift (again, only the range between $\sigma_{\min}$ and $\sigma_{\max}$). This results in a fitting procedure as depicted in Figure 3b.

3.3.3. Error Metrics

Two error metrics are used to assess the goodness of the fits, both relying on the absolute and relative errors between the prediction value from the model σ_{sim} and the true value from experimental data σ_{exp}. The relative error is the absolute error divided by the mean of the experimental error $\overline{\sigma}_{\text{exp}}$, as follows:

$$e_{\text{abs}} = \sigma_{\text{sim}} - \sigma_{\text{exp}} \tag{5}$$

$$e_{\text{rel}} = \frac{e_{\text{abs}}}{\overline{\sigma}_{\text{exp}}} \tag{6}$$

The first metric is the maximum error defined in relative form as follows:

$$e_{\text{rel}}^{\max} = \max(e_{\text{rel}}). \tag{7}$$

In addition to the relative maximum error, the corresponding absolute value is calculated to provide an absolute measure. The absolute maximum value is the absolute error at the same location where the relative error is the largest, as follows:

$$e_{\text{abs}}^{\max} = e_{\text{abs}}\Big|_{e_{\text{rel}}=e_{\text{rel}}^{\max}} \tag{8}$$

The second metric is the root-mean-squared error (RMSE) in absolute form, defined as follows:

$$e_{\text{RMS}} = \sqrt{\frac{1}{N}\sum_{i=1}^{N}(e_{\text{abs}})^2}. \tag{9}$$

Here, N is the length of the absolute error, i.e., the number of entries in its vector. The RMSE can also be calculated in a relative manner for comparative purposes as normalized root-mean-squared error (NRMSE), defined by the following:

$$e_{\mathrm{NRMS}} = \frac{e_{\mathrm{RMS}}}{\overline{\sigma}_{\mathrm{exp}}}. \tag{10}$$

4. Results and Discussion

An overview of all 27 conducted tests, showing all 10 conducted cycles per test in a stress–strain diagram, is given in Figure 4. Four aspects should be noted that hold true for Figure 4 as well as for the remainder of the text, unless stated otherwise:

(1) The data shown and discussed have been corrected for the stiffness of the UTM, as described in the experimental Section 2.2.
(2) The stress–strain relationship was mirrored to the first quadrant for readability, resulting in a positive sign for compressive stresses and strains.
(3) Anode data are shown in red, cathode data are shown in blue, and separator data are shown in green.
(4) Different compression rates of 1C, 3C, and 5C are shown using different color brightness levels.

From the results in Figure 4, the cathode is the stiffest component, closely followed by the anode. The separator is more compliant by a factor of approximately five than the electrode materials. This trend holds true regardless of the nominal stress and compression rate. When comparing the results with data from the literature, several similarities and differences can be observed. For example, Sauerteig et al. [1], Aufschläger et al. [9], and Schabenberger et al. [11] report that the separator is the most compliant component, with similar strains between 10% and 16% for stresses between 1.75 MPa and 3.0 MPa. The cathode tends to be the stiffest component, and the anode stiffness typically falls between those of the cathode and the separator. Comparing this general behavior to the first compression step of our data, the same trend and similar absolute values can be found. However, only the first compression step can be used for this comparison. On the one hand, this is because sometimes the literature [9] does not provide decompression behavior. On the other hand, the final decompression from Figure 4 is most likely influenced by the mechanical cycles between compression and decompression, making a direct comparison to literature without mechanical cycles [1] difficult. This is due to plastic behavior, as will be discussed later. Nonetheless, all results throughout the literature consistently show a strain-hardening effect, which will also be discussed in more depth later. It should be noted that the literature might also show data at largely different stress levels, e.g., [4,6,7]. This results in largely different strain ranges, making a direct comparison to our results difficult.

Overall, the literature shows similar trends regarding the initial compression behavior when compared to the results presented here. In the following sections, the stress–strain relationship from Figure 4 is analyzed to understand the evolution during mechanical cycling by investigating the plastic deformation, as well as to determine the presence of pressure-dependency and/or rate-dependency by investigating the maximum total strain. Finally, a linear-elastic model and a poroelastic material model are fitted to the experimental data to answer the question of whether a material model can be utilized to describe the mechanical behavior, and if so, which is suitable. It should already be noted that the poroelastic model described in this paper represents a snapshot of the mechanically settled state and, therefore, does not account for plastic or aging processes.

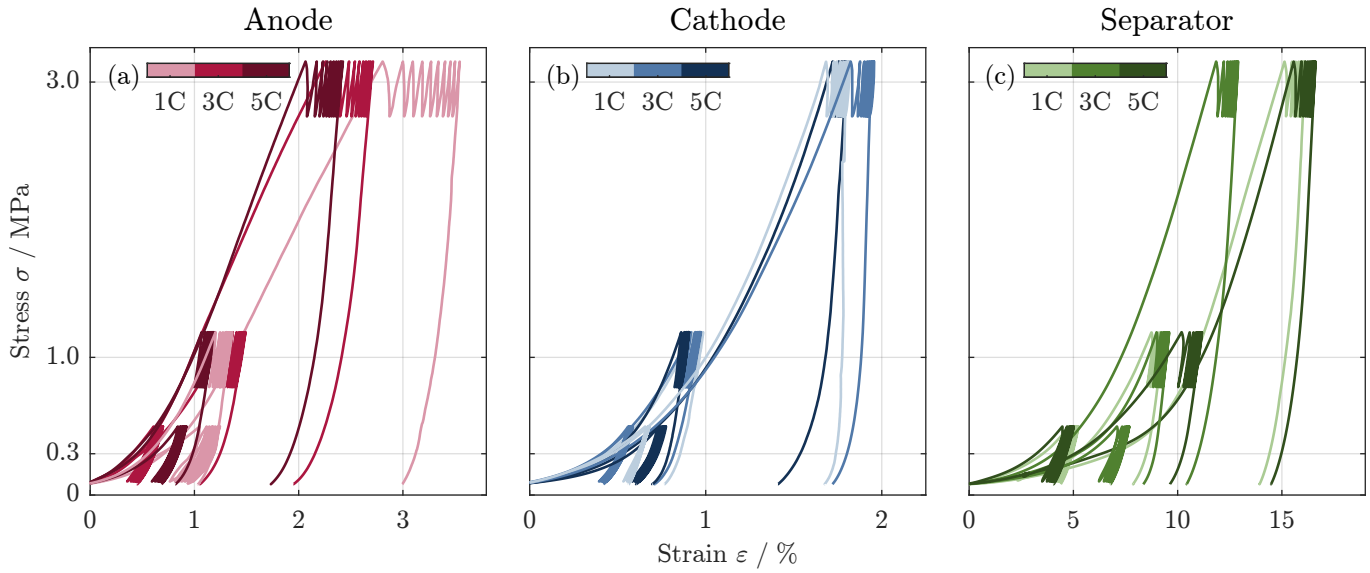

Figure 4. Overview of all conducted compression tests with (**a**) anodes, (**b**) cathodes, and (**c**) separators is shown using stress–strain diagrams. Positive values indicate compressive behavior. The gradient color bar indicates the different compression rates v of 1C, 3C, and 5C, which are to be interpreted as equivalent current rates and are further defined in the last row of Table 1.

4.1. Compression Tests

In general, solidification is the process by which a material's strength increases during plastic deformation [50]. In a stress–strain diagram, this becomes evident by a steeper slope. This observation can also be made for the data in Figure 5; the data exemplary show the separator at a compression rate of $v = 1\text{C}$ and nominal stress of $\sigma_{\text{nom}} = 1.0\,\text{MPa}$, as seen in Figure 4. Upon closer inspection of this magnified section, a distinct difference in the slope of the first compression cycle can be observed compared to the subsequent cycles. This change in slope suggests that the material undergoes a solidification process, resulting in an increase in stiffness with an increasing cycle number. This solidification phenomenon is observed consistently across all the tested conditions, although the example provided in Figure 5 is presented as a representative case. Figure 5 also highlights selected data points from which the plastic strain of each cycle can be calculated. The plastic strain $\varepsilon_{\text{plast}}$ is defined as the irreversible strain when comparing the end of the decompression $\varepsilon_{\text{min},i+1}$ with the beginning of the compression $\varepsilon_{\text{min},i}$ of a given mechanical cycle i.

$$\varepsilon_{\text{plast}} = \varepsilon_{\text{min},i+1} - \varepsilon_{\text{min},i} \tag{11}$$

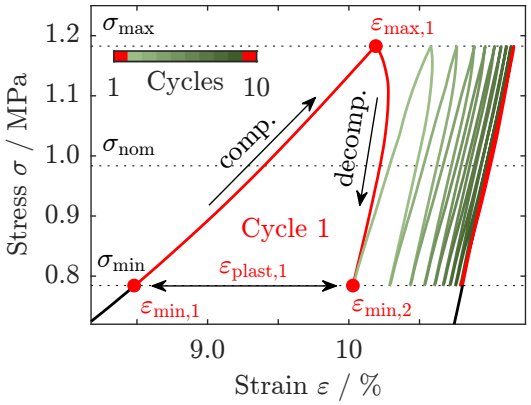

Figure 5. Separator data from Figure 4 at $v = 1\text{C}$ and $\sigma_{\text{nom}} = 1.0\,\text{MPa}$, magnified to show the operating window. In addition to the data, further information is also displayed to visualize the definition of the plastic strain.

The plastic strain from Equation (11) is then used to investigate the behavior during mechanical cycling in Figure 6. The three columns show the data for the anode, cathode, and separator data, respectively. The three rows show the data at different nominal stresses. Some data points are omitted because the logarithmic scale of the abscissa cannot show negative values. Negative values arise when the plastic strain of cycle $i + 1$ is less than that of cycle i.

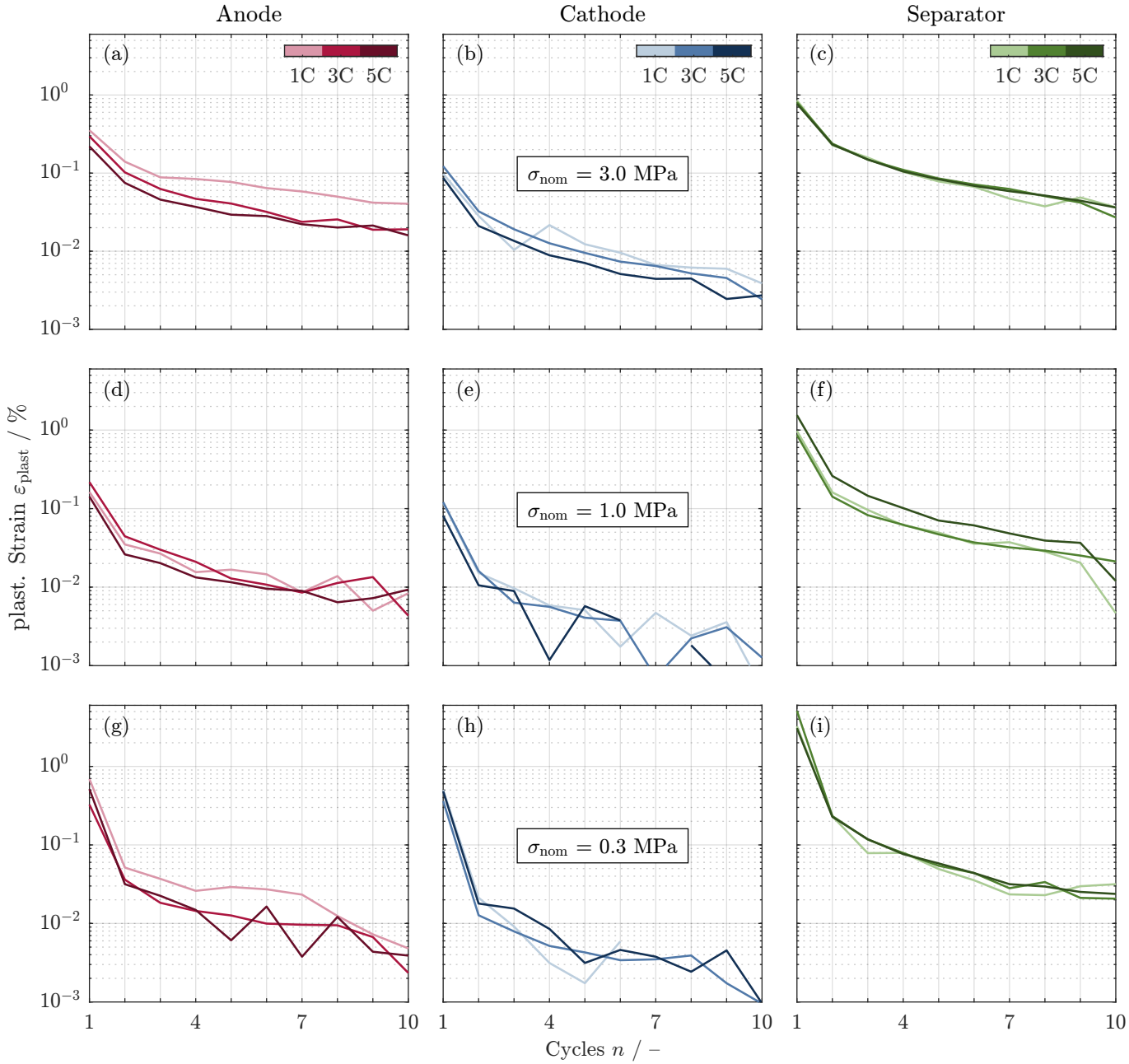

Figure 6. Evolution of plastic strain $\varepsilon_{\text{plast}}$ as defined by Equation (11) over mechanical cycling. Columns show the data for the anode in (**a**,**d**,**g**), the cathode in (**b**,**e**,**h**), and the separator in (**c**,**f**,**i**), respectively. The first, second, and third rows show the data at nominal stresses σ_{nom} of 3.0 MPa, 1.0 MPa, and 0.3 MPa, respectively. Some data points are omitted because the logarithmic scale of the abscissa cannot show negative values.

Throughout all data shown in Figure 6, the first cycle exhibits the largest plastic deformation, which then decreases with the increasing cycle number. This transition from plastic to elastic behavior is fastest for the cathode material, followed by the anode and then the separator material. After 10 cycles, the plastic strain for all tests is less than a tenth of the value of the first cycle. In absolute terms, the plastic strain after 10 cycles is less than 0.04%. This suggests that using a single mechanical compression and decompression step as usually done in the literature (see Table 1) is not sufficient to characterize the mechanical behavior of the sample under operating conditions.

When comparing all nine data lines within one column of Figure 6, no significant difference in the change of plastic strain with respect to the nominal stress (rows) or with respect to the compression rate (color brightness) can be observed. This suggests that the stiffening behavior during mechanical cycling within the operating window is independent of both, the absolute stress and the compression rate.

The observed plastic effects can potentially be attributed to various microstructural changes and reorganizations within the electrode and separator materials induced by the compressive stresses. The increase in stiffness with successive compression cycles is likely due to a strain hardening effect [51,52], where the compressive stresses drive the reorganization and strengthening of the internal microstructure and bonding within the materials, as Wen et al. [53] reported. Furthermore, the decrease in plastic strain with the increasing cycle number suggests that the materials experience irreversible plastic deformation during the initial cycles. The materials may also exhibit time-dependent viscoelastic behavior [54,55]. These time-dependent deformation mechanisms can lead to changes in the overall stress–strain response. However, the effects of time-dependent behavior have not been investigated in the present work. To further investigate these potential mechanisms, additional experiments could be of great interest, e.g., in-operando microscopy or X-ray imaging, hold phases or creep tests, or statistical testing for dependencies on temperature or compression rates.

Complementary to the findings on plastic strain evolution, Figure 7 shows the maximum absolute strain of each of the 27 tests, i.e., it shows $\varepsilon_{\mathrm{max},10}$ for the 10th cycle, analogous to what is shown in Figure 5. The maximum strain exhibits a positive correlation with increasing nominal stress. At closer inspection, Figure 7 supports the findings from Figure 6, i.e., that no clear dependency on the compression rate can be found. However, a differentiation between the different components is possible. The separator shows the greatest maximum strain throughout all data. Anode and cathode data are comparable in terms of maximum strain, while the cathode tends to show lower maximum strains at the same applied pressure, resulting in a stiffer material. These statements largely hold true even when accounting for the largest error to be expected, as indicated by the error bars in Figure 7. The error bars are based on the standard deviation $S = 0.19\%$ of six measurement repetitions using cathode samples at $\sigma_{\mathrm{nom}} = 1.0\,\mathrm{MPa}$ and $v = 1\mathrm{C}$. Since the cathode is the stiffest material, the largest error is to be expected here, and the same standard deviation is also used for the other error bars. More information and data regarding the six repetitions can be found in Appendix A.

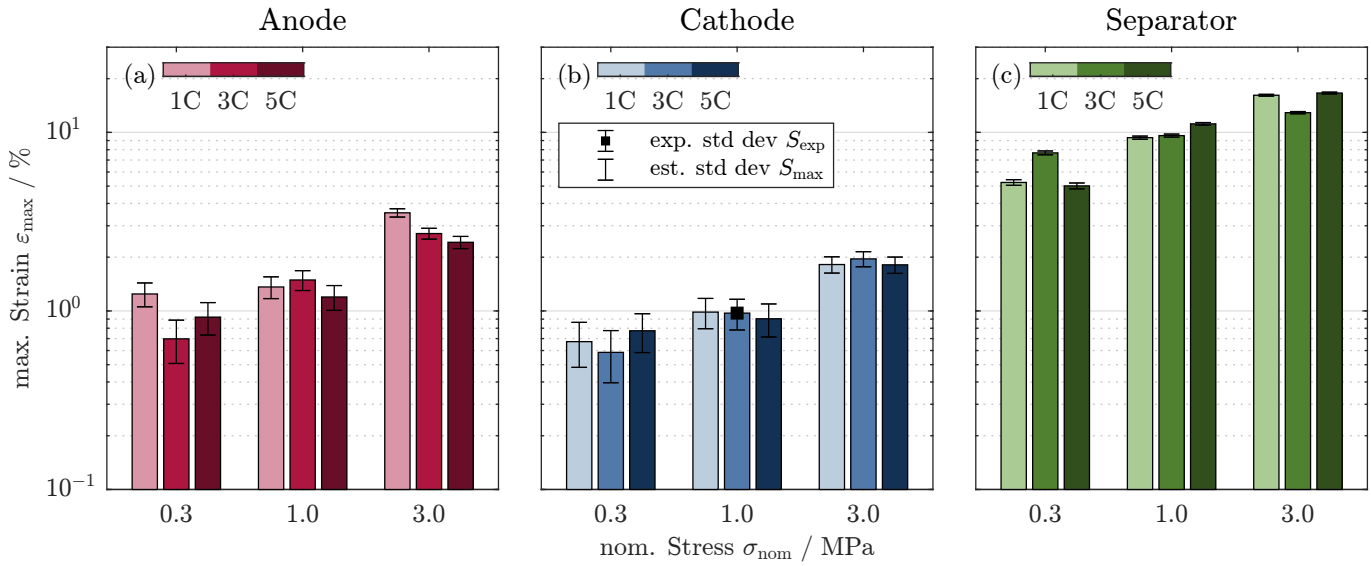

Figure 7. Influence of the compression rate v (1C, 3C, 5C) and nominal stress σ_{nom} (0.3 MPa, 1.0 MPa, 3.0 MPa) on the maximum strain $\varepsilon_{max,10}$ of the 10th cycle for the (**a**) anode, (**b**) cathode, and (**c**) separator. The error bars shown are based on the standard deviation $S = 0.19\%$ from 6 experimental repetitions at 1.0 MPa and 3C using cathode samples. The black square indicates the measurement point for the repetitions, while error bars without a marker utilize the same standard deviation since it is the largest error to be expected. More information can be found in the Appendix A.

It should be noted that although no clear rate dependency can be observed here, reports on a rate dependency can be found in the literature. For example, Ding et al. [7] investigated a PE as well as a polypropylene (PP) separator. They report a similar dependency on the strain rate for both materials, with stiffer material behavior at higher strain rates. Experiments were conducted with electrolyte-filled samples of a 10 mm diameter. Kalnaus et al. [5] investigated a triple layer PP-PE-PP separator at dry conditions and a 20 mm diameter. At similar compression rates, they report the same dependency as Ding et al. [7]. The separators in the present study are made of PE, too, and the strain rate used here is within the range used by [5,7]. Dry conditions and a diameter of 18 mm are similar to [5]. However, no clear rate dependency can be observed. It is suspected that the rate dependency is not clearly visible for two reasons. On the one hand, the stress levels used here are only at 3.0 MPa, while [5,7] conducted their tests up to 150 MPa. This results in a largely different strain value of approx. 15% compared to 80%. It might be that the rate dependency is not as pronounced at rather low absolute pressures as it is at high pressures. On the other hand, the literature tested a broader range of strain rates that differs by several orders of magnitude compared to what is tested here (see Table 1). This rather narrow range combined with the lower stress levels used for the present study might be the reason behind the seemingly missing rate dependency. However, since the stress levels and compression rates are chosen to be representative of typical battery cycling, these results suggest that the rate dependency reported in the literature might not be relevant to normal battery operation.

4.2. Modeling

This section explores whether the mechanical behavior can be described by a material model. To this end, two different material models were fitted to the compression steps of each cycle for each of the 27 tests. At first, the experimental data of each compression step are zeroed so that the compression data used for the fit start at $(\varepsilon, \sigma) = (0, 0)$, as visualized in Figure 3a. If this was not the case, the linear-elastic model, in particular, would represent the behavior between $(0, 0)$ and $(\varepsilon_{max,i}, \sigma_{max})$; however, the actual operating window is located between $(\varepsilon_{min,i}, \sigma_{min})$, and $(\varepsilon_{max,i}, \sigma_{max})$. For a meaningful comparison of both

material models, the shifted data are also used to fit the poroelastic model. Afterward, the poroelastic model is also fit to the original data without any translation to account for the absolute stress and strain values and not only the change within the operating window. The initial stress σ_0 is set to zero when fitting the poroelastic model.

Figure 8 shows Young's modulus from Equation (2), calculated for the compression step of each test plotted against the number of cycles. The results show that Young's modulus increases with the increasing number of cycles, but approaches a constant value, indicating a solidification process. The overall behavior is similar regardless of the compression rate (see same line styles). However, a dependency on the nominal stress can be observed. Young's modulus increases with higher nominal stress, resulting in stiffer material behavior. These findings from the linear-elastic model are consistent with the observations in Figure 6; the first cycle exhibits significantly different behavior than the following cycles, suggesting that a single compression and decompression step is not sufficient to characterize the mechanical behavior for the given operating window.

Figure 9 evaluates the goodness of the fits through true-predicted diagrams for both the linear-elastic model and the poroelastic model, using lighter colors for the linear-elastic model and darker colors for the poroelastic model. Each panel displays the data for 10 cycles at 3 compression rates for both material models, resulting in 30 light and 30 dark lines. The ordinate shows the true stress as measured from the experiments, while the abscissa shows the predicted stress from either model at the given experimentally measured strain. The dashed black lines indicate an error of predicted stress (abscissa) of $\pm 5\%$ relative to the experimental stress (ordinate). Individual cycles or compression rates are not distinguished by a color gradient, but the overall behavior with increasing cycle numbers is indicated by the two arrows in panel h). The data in Figure 9 show that the linear-elastic model yields larger errors than the poroelastic model for all nine panels. Additionally, the linear-elastic model tends to have a rather curved shape, overestimating the stress at low experimental stress and underestimating the stress at high experimental stress, resulting in a non-linear error behavior. The final fit results, as well as error quantities for the linear-elastic model, are given in Table A1. The overall NRMSE for the linear model in the 10th cycle is $\leq$24.88% ($\leq 49.43 \times 10^{-3}$ MPa).

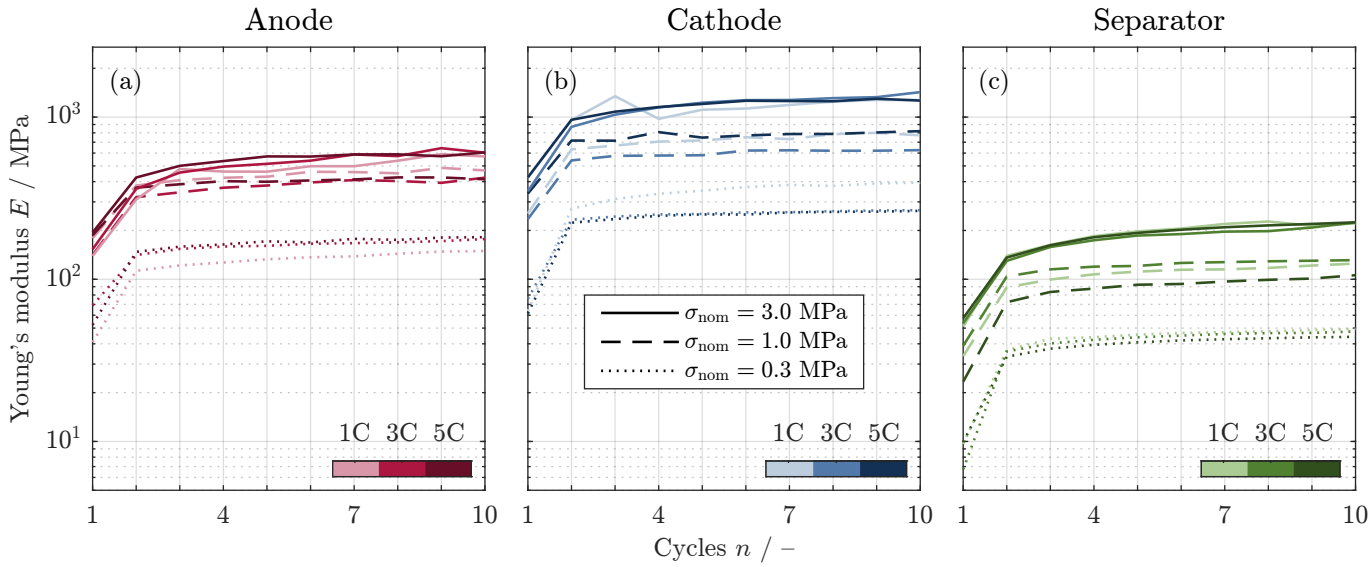

Figure 8. Evolution of Young's modulus E throughout the mechanical cycling for (**a**) anode, (**b**) cathode, and (**c**) separator. Evaluation was performed for the compression of each cycle as depicted in Figure 3a. The nominal stress σ_{nom} is indicated by different line styles, and the compression rate v is denoted by different color brightnesses.

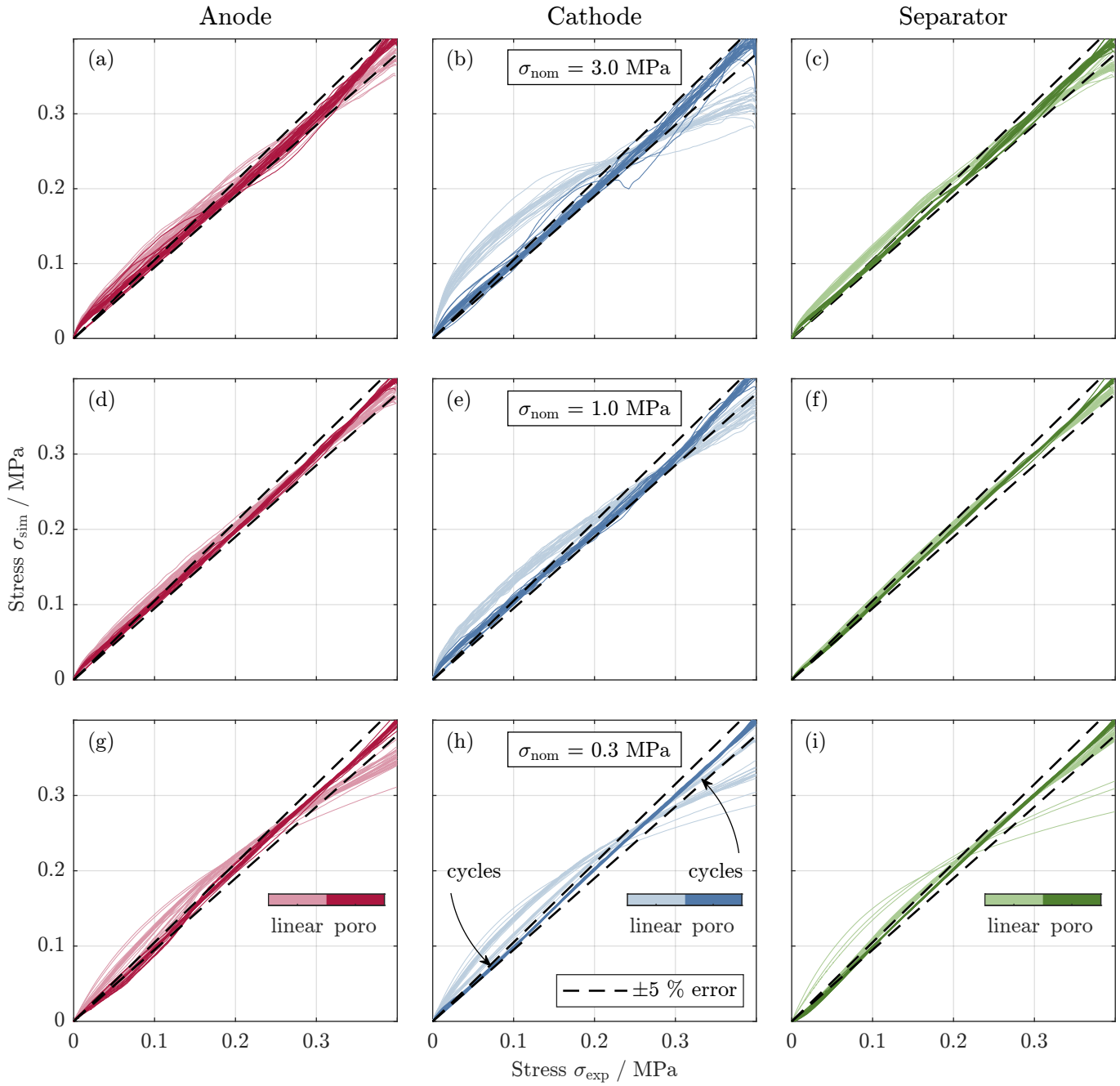

Figure 9. Goodness of the linear-elastic and poroelastic modeling approach from Figure 3a for all 10 cycles. Goodness is evaluated using true-predicted diagrams, which include the simulated stress data from the model σ_{sim} versus the experimental stress data σ_{exp}, respectively, for all compression rates v in the case of compression. Columns show the data for the anode in (**a**,**d**,**g**), the cathode in (**b**,**e**,**h**), and the separator in (**c**,**f**,**i**), respectively. Each panel displays the data for 10 cycles at 3 compression rates for both material models, resulting in 30 light and 30 dark lines.

In contrast to the linear-elastic model, the poroelastic model in Figure 9 predominantly falls within the ±5% error margin. One exception to this can be found in the cathode data at 3.0 MPa of nominal stress in panel b. Here, the data for the poroelastic model show fluctuations, especially around $\sigma_{exp} = 0.2$ MPa, which cannot be seen in any other panel. Overall, the poroelastic material model outperforms the linear-elastic model, especially for small nominal stresses. This might be particularly relevant when modeling the mechanical behavior at begin of life when absolute pressures are low. For example, if degradation models were dependent on mechanical stress, deviations in the stress would result in an overestimation or underestimation of the degradation. The final fit results as well as error quantities for the poroelastic model with translated data are given in Table A2. The poroelastic model reduces the NRMSE in the 10th cycle from ≤24.88% (≤49.43 × 10^{-3} MPa) for the linear model to correspondingly ≤7.26% (≤14.46 × 10^{-3} MPa).

Figure 10 shows the results when fitting the experimental data as visualized in Figure 3b. Again, the ordinate shows the experimentally measured stress, while the abscissa shows the predicted stress at any given strain. Only the compression step of the 10th cycle is shown. The black dashed and dotted lines indicate a relative error of ±5% and ±1%, respectively. Note that the error definition is the same as in Figure 9, i.e., the error indicators are given relative to the experimentally measured stress on the ordinate. The results in Figure 10 show an overall small error <±5%, except for small absolute stresses, as can be seen in panels (g) through (i). Again, this can be explained by small absolute values used as a reference when calculating the error. For nominal stresses of 1.0 MPa and 3.0 MPa, the error decreases to < ±1%, except for the cathode data, with a nominal stress of 3.0 MPa in panel (b). This could be explained by the fact that the cathode is very stiff but still exhibits a non-linear stress–strain relationship in the range of 3.0 MPa. A similar curved shape to the one seen in panel (b) can also be observed in panels (a) and (c), although it is less distinct. Lastly, these observations hold true for all three tested compression rates, as no dependency on the compression rate can be seen. The final fit results as well as error quantities for the poroelastic model without translation are given in Table A3. The NRMSE in the 10th cycle is overall ≤5.47% (≤31.20 × 10^{-3} MPa).

When comparing the two poroelastic modeling approaches from panels a and b in Figure 3, the results in Figures 9 and 10 seem similar at first. For higher nominal stresses of 1.0 MPa and 3.0 MPa, in particular, the error characteristics are almost identical. At low nominal stresses of 0.3 MPa, the poroelastic model, including the translation of data, shows better prediction capability for the 10th cycle. However, the differences are less than ±5%-points in NRMSE for almost all cases. Furthermore, the model fitted to translated data can only capture the change in mechanical stress and strain within the operating window, while the model fitted to the data without translation also accounts for the absolute values of stress and strain. Because of this, the second modeling approach without translation is deemed superior.

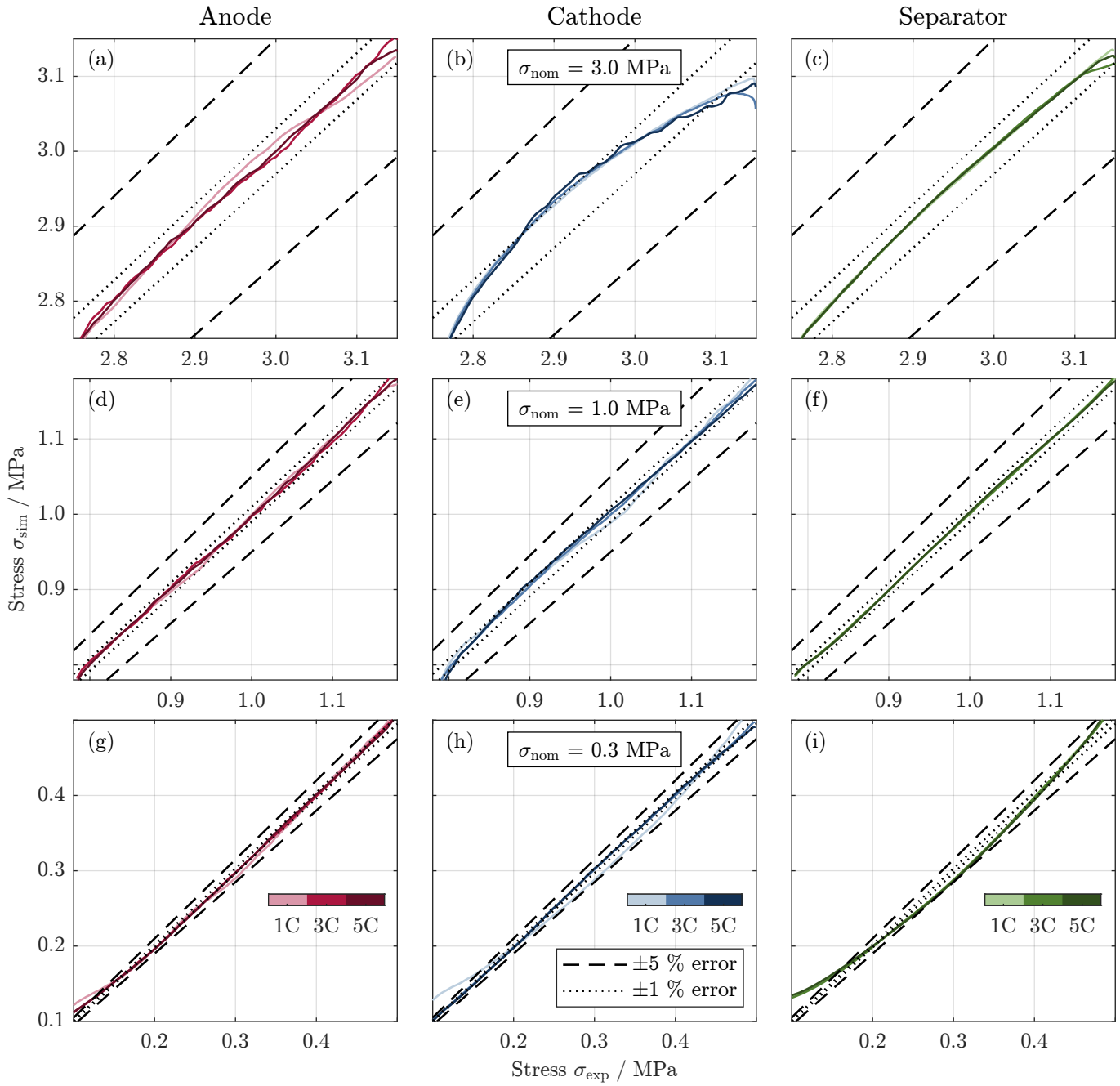

Figure 10. Goodness of the poroelastic modeling approach from Figure 3b for the 10th cycle. Goodness is evaluated using true-predicted diagrams, which include the simulated stress data from the model σ_{sim} versus the experimental stress data σ_{exp}, respectively, for all compression rates v in the case of compression. Columns show the data for the anode in (**a**,**d**,**g**), the cathode in (**b**,**e**,**h**), and the separator in (**c**,**f**,**i**), respectively. Each panel displays the data only for the 10th cycle at 3 compression rates for the poroelastic material model only, resulting in 3 lines.

5. Conclusions

The results and discussion sections address several key research questions regarding the mechanical behavior of lithium-ion battery components under cyclic compression:

– *Compression rate dependency.* The results do not support any dependency of the mechanical behavior on the compression rate v (1C, 3C, 5C) for a given nominal stress σ_{nom}. The stiffening behavior during cycling was found to be independent of the compression rate.

- *Nominal stress dependency.* The mechanical behavior was found to be dependent on the nominal stress σ_{nom} (0.3 MPa, 1.0 MPa, 3.0 MPa). Higher nominal stresses σ_{nom} resulted in stiffer material behavior, as evidenced by higher values in Young's modulus E.
- *Cyclic behavior.* The mechanical behavior was found to be highly dependent on the number of cycles. The first cycle exhibited the largest plastic deformation, which then decreased rapidly with the increasing cycle number. After 10 cycles, the plastic strain was less than 0.04% for all tests, suggesting that a single compression–decompression step may not be sufficient to characterize the mechanical behavior under operating conditions.
- *Compression/decompression behavior.* The results show a clear distinction between the compression and decompression behavior during the first few mechanical cycles. However, after 10 cycles, the distinction vanished.
- *Material modeling.* Two material models, a linear-elastic and a poroelastic model, were fitted to the experimental data. The poroelastic model outperformed the linear-elastic model, especially at low nominal stresses, providing a better description of the mechanical behavior. The poroelastic model fitted to the original data without translation showed superior performance, as it could capture both the changes in mechanical stress and strain within the operating window, as well as the absolute values of stress and strain.

In conclusion, the study provides valuable insights into the complex mechanical behavior of lithium-ion battery components under cyclic compression. The findings highlight the importance of considering the evolution of mechanical properties during cycling, the influence of nominal stresses, and the suitability of the poroelastic model for describing the observed behavior. These insights can contribute to the development of more accurate mechanical models for lithium-ion batteries, which are crucial for predicting degradation and improving battery design and performance.

Furthermore, the introduced method can be applied to a variety of lithium-ion battery systems and scenarios. Some key aspects of its versatility include the following:

- *Different charge/discharge rates.* The method can be used to investigate the mechanical behaviors of electrodes under various charge and discharge rates, reflecting different operating strategies and power requirements.
- *Varying temperature ranges.* By incorporating active temperature control or testing in different climatic zones, the method can be used to study the impact of temperature on the mechanical properties of electrodes across a wide range of operating conditions.
- *Other cell geometries.* As long as the electrode samples can be prepared in a coin cell format, the method can be applied to cells of different sizes. However, the applicability for wound cell geometries may be limited due to the uniaxial assumption of the model.
- *Higher stress levels.* The method can be used to investigate the mechanical behavior of electrodes under higher stress levels, which can be influenced by the depth of discharge (DoD) window during operation.
- *Hold phases.* The impact of hold phases with constant stress, as determined by the operating strategy, on the mechanical properties of electrodes can also be studied using the introduced method.
- *Aged samples.* The method can potentially be used to study the mechanical characteristics of electrodes at different stages of real-world aging, which can be influenced by external factors. If material properties should not change during aging, this might indicate that testing aged materials is not required, speeding up the parametrization process.

  It is important to note that the versatility of the method is primarily limited by the ability to prepare the samples in a coin cell format. Samples with more brittle characteristics, such as all-solid-state battery (ASSB) materials, may be challenging to test using this approach due to their inherent material properties.

Future work (apart from the aforementioned aspects) could address several research questions derived from the proposed testing procedure and findings of this study. The setup could be modified to cover two aspects. On the one hand, it could be adapted so that samples wetted with electrolytes can also be tested to investigate the influence of electrolytes on mechanical behavior. On the other hand, the setup could be extended by external displacement sensors to increase the precision of the measurement, similar to what Spielbauer et al. [4] have shown. Additionally, the mechanical behavior at different states of charge should be investigated to enable a more precise prediction of the mechanical behavior. This is especially important for predicting the reversible mechanical behavior during cycling. Lastly, harvesting electrodes at different points during the lifetime of a battery to investigate the aged cell would allow for a comparison between the predicted mechanical behavior and the true mechanical behavior at different states of health. If the predictions at the beginning of life accurately fit the true behavior at the end-of-life, long-term and cost-intensive aging tests might not be required anymore.

Author Contributions: Conceptualization, J.B.; methodology, J.B. and A.D.; software, J.B. and T.K.; validation, J.B. and A.D.; formal analysis, J.B. and T.K.; investigation, J.B. and T.K.; resources, P.K. and M.A.; data curation, J.B. and T.K.; writing—original draft preparation, J.B. and A.D.; writing—review and editing, T.K., P.K., M.A. and A.J.; visualization, J.B., A.D., T.K., P.K., M.A. and A.J.; supervision, P.K., M.A. and A.J.; project administration, A.J. All authors have read and agreed to the published version of the manuscript.

Funding: This work was funded by the BMW AG and was performed in cooperation with the Chair of Electrical Energy Storage Technology at the Technical University of Munich.

Data Availability Statement: The datasets presented in this article are not readily available due to the BMW AG confidentiality guidelines. Requests to access the datasets should be directed to BMW AG.

Acknowledgments: The authors would like to thank our colleagues Marlene Zink (BMW AG) and Maria Hilzinger (BMW AG) for conducting SEM imaging and helium pycnometer measurements for material characterization.

Conflicts of Interest: Authors Johannes Brehm, Tobias Kussinger, Philip Kotter and Maximilian Altmann were employed by the company Bayerische Motoren Werke Aktiengesellschaft (BMW AG). Authors Axel Durdel and Andreas Jossen were employed by the Technical University of Munich (TUM). All authors declare that the research was conducted in the absence of any commercial or financial relationships that could be construed as a potential conflict of interest.

Abbreviations

The following abbreviations are used in this manuscript:

Acronyms

ASSB	all-solid-state battery
BoL	begin of life
DoD	depth of discharge
DoL	degree of lithiation
EoL	end of life
EV	electric vehicle
FT-IR	Fourier transform infrared spectroscopy
Gr	graphite
ICP-OES	inductively coupled plasma-optical emission spectrometry
LCO	lithium-cobalt-oxide
NCA	nickel-cobalt-aluminum
NMC	nickel-manganese-cobalt
NRMSE	normalized root-mean-squared error
PE	polyethylene

PP	polypropylene
RMSE	root-mean-squared error
SEM	scanning electron microscopy
Si	silicon
SoC	state of charge
STA-MS	simultaneous thermal analysis with mass spectroscopy
UTM	universal testing machine

Roman Symbols

$\boldsymbol{C}$	elasticity tensor, Nm^{-2}
E	Young's modulus, Nm^{-2}
e	error
G	shear modulus, Pa
h	sample height, m
$\mathbb{I}$	identity matrix,
J	volume ratio,
K	bulk modulus, Pa
L	through-plane thickness, m
n	number of cycles, 1
p	pressure, Pa
S	standard deviation
V	volume, m^3
v	compression rate, MPah^{-1}

Greek Symbols

ϵ	volume fraction, 1
ε	strain, 1
$\boldsymbol{\varepsilon}$	strain tensor, 1
κ	logarithmic bulk modulus, 1
ν	Poisson's ratio, 1
σ	stress, Nm^{-2}
$\boldsymbol{\sigma}$	stress tensor, Nm^{-2}

Subscripts & Superscripts

0	stress-free state
1	pre-load state
abs	absolute
ax	uniaxial
el	elastic component
exp	experimental
l	liquid phase
max	maximum
min	minimum
nom	nominal
NRMS	normalized root-mean-squared value
plast	plastic
rel	relative
RMS	root-mean-squared value
s	solid phase
sim	simulated
t	tensile
tot	total
vol	volumetric

Appendix A. Precision of Strain Measurement

To evaluate the precision of strain measurement and the resulting error thereof, 6 repetitions at one of the 27 measurement points have been conducted. Since the cathode shows the stiffest behavior, the smallest absolute change in thickness is to be expected, resulting in the largest signal-to-noise ratio. Consequently, tests using cathode materials will yield the largest error to be expected.

Figure A1 shows the results of these 6 repetitions at $\sigma_{\text{nom}} = 1.0\,\text{MPa}$ and $v = 1\text{C}$ as (a) a stress–strain diagram as well as (b) the evolution of the plastic strain with the increasing cycles, analogous to Figures 4 and 6. The evolution of the plastic strain in Figure A1b reveals that all 6 repetitions show similar behavior, almost identical to that shown in Figure 6e.

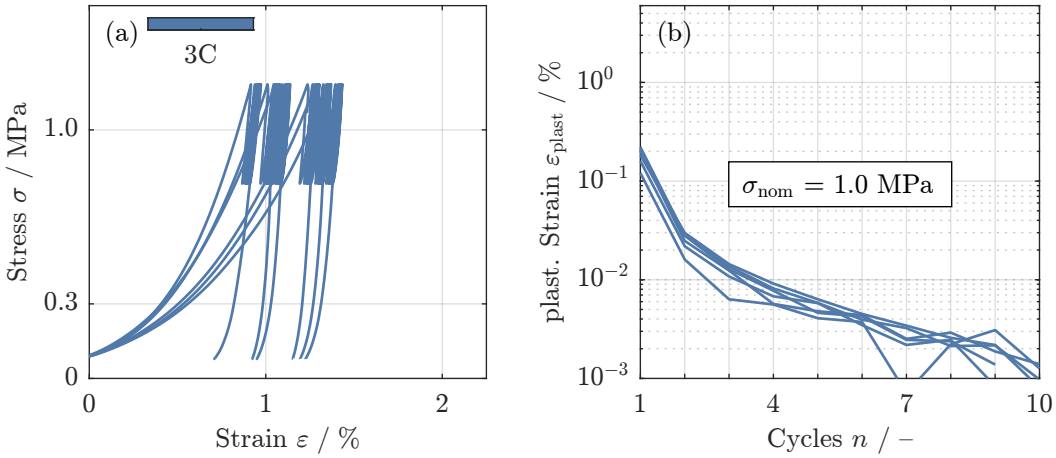

Figure A1. Precision of the strain measurement shown for the cathode at a stress level σ_{nom} of 1.0 MPa and a compression rate v of 1C by: (**a**) An overview of 6 compression test repetitions, where a standard deviation of $S = 0.19\%$ of the ε_{max} can be observed (in addition to Figure 4) and (**b**) the evolution of plastic strain $\varepsilon_{\text{plast}}$ as defined by Equation (11) over mechanical cycling for six compression test repetitions (in addition to Figure 6).

To further allow for an estimate of the error in the 10th cycle, the standard deviation in the maximum strain was evaluated to be $S = 0.19\%$. This standard deviation is used as error bars in Figure 7. The error bar with the black central square indicates the measurement point for which the six repetitions had been conducted. Since the cathode is the stiffest material, this standard deviation is the largest to be expected. To allow for a maximum error estimate, error bars based on the same standard deviation have been added to all other data bars in Figure 7 (no central black squares).

Appendix B. Detailed Modeling Equations

Appendix B.1. Hooke's Law in Matrix Form

Hooke's law for isotropic materials in compliance matrix form (Voigt notation) is given by the following:

$$\underbrace{\begin{bmatrix}\sigma_{11}\\ \sigma_{22}\\ \sigma_{33}\\ \sigma_{23}\\ \sigma_{13}\\ \sigma_{12}\end{bmatrix}}_{\boldsymbol{\sigma}}^{\text{el}} = \underbrace{\frac{E}{(1+\nu)(1-2\nu)} \cdot \begin{bmatrix} 1-\nu & \nu & \nu & 0 & 0 & 0\\ \nu & 1-\nu & \nu & 0 & 0 & 0\\ \nu & \nu & 1-\nu & 0 & 0 & 0\\ 0 & 0 & 0 & \frac{1-2\nu}{2} & 0 & 0\\ 0 & 0 & 0 & 0 & \frac{1-2\nu}{2} & 0\\ 0 & 0 & 0 & 0 & 0 & \frac{1-2\nu}{2} \end{bmatrix}}_{\boldsymbol{C}} \cdot \underbrace{\begin{bmatrix}\varepsilon_{11}\\ \varepsilon_{22}\\ \varepsilon_{33}\\ 2\varepsilon_{23}\\ 2\varepsilon_{13}\\ 2\varepsilon_{12}\end{bmatrix}}_{\boldsymbol{\varepsilon}}^{\text{el}} \tag{A1}$$

where Young's modulus E can be alternatively expressed through the shear modulus G or the bulk modulus K and Poisson's ratio ν:

$$E = 2G(1+\nu) = 3K(1-2\nu) \tag{A2}$$

Appendix B.2. Derivation of the Poroelasticity

Due to the morphological similarity of the porous materials of a lithium-ion cell and the porous layers in the soil, this work uses an approach from soil modeling, which

was mentioned for the first time in a similar form in [48] and later recommended by [49] for modeling poroelastic material behaviors. The adopted approach (Equation (A3)) is a differential relation that describes a linear elastic change in the void-to-solid ratio $\epsilon_{l/s}$ (Equation (A4)) due to a logarithmic change of the applied pressure p (Equation (A5)). Here, κ denotes the logarithmic bulk modulus, which is subsequently used as one of two parameters for the model fitting, and p_t^{el} describes the elastic tensile strength of the porous material. It is assumed that the compressibility of the solid phase can be neglected: $V_s^{el} = V_s^0 = V_s$. This assumption is considered admissible because the mechanical stresses that occur in the electrodes due to external stress typically do not exceed the strength of the active material or particles [56]. V_s denotes the solid volume, and V_l denotes the pore volume, which is interpreted as the liquid volume of the electrolyte in the porous matrix of a lithium-ion cell.

$$d\epsilon_{l/s}^{el} = -\kappa \cdot d \ln\left[p + p_t^{el}\right] \tag{A3}$$

$$\epsilon_{l/s} = \frac{V_l}{V_s} \tag{A4}$$

$$p = -\frac{1}{3}\mathrm{trace}(\sigma) = -\frac{1}{3}\sigma : \mathbb{I} \tag{A5}$$

The void-to-solid ratio in the initial configuration $\epsilon_{l/s}^0$ can then be written as a function of the initial porosity ϵ_l^0 using the definition from Equation (A4). Accordingly, the void-to-solid ratio in the elastically deformed configuration $\epsilon_{l/s}^{el}$ would depend on the porosity in the deformed configuration. However, this porosity is typically unknown.

$$\epsilon_{l/s}^0 = \frac{V_l^0}{V_s^0} = \frac{\epsilon_l^0}{1 - \epsilon_l^0} \tag{A6}$$

Using the elastic change in the void-to-solid ratio, the elastic volume change J^{el} can be written as follows:

$$J^{el} = \frac{1 + \epsilon_{l/s}^{el}}{1 + \epsilon_{l/s}^0} = \frac{1 + \frac{V_l^{el}}{V_s}}{1 + \frac{V_l^0}{V_s}} = \frac{V_s + V_l^{el}}{V_s + V_l^0} = \frac{V_{tot}^{el}}{V_{tot}^0} = 1 + \varepsilon_{vol}^{el} \tag{A7}$$

Here, V_l^0 denotes the initial pore volume, V_l^{el} denotes the pore volume after elastic deformation. The same applies to the total volume V_{tot}^0 and V_{tot}^{el}, respectively. Integrating the differential relation from Equation (A3), substituting Equation (A7), and choosing the integration constant so that $p(\varepsilon_{vol}^{el} = 0) = 0$ yields the following:

$$\frac{\kappa}{1 + \epsilon_{l/s}^0} \cdot \ln\left[\frac{p + p_t^{el}}{p_0 + p_t^{el}}\right] = 1 - J^{el} = -\varepsilon_{vol}^{el} \tag{A8}$$

Equation (A8) can finally be solved for the pressure:

$$p = \left(p_0 + p_t^{el}\right) \cdot \exp\left[-\varepsilon_{vol}^{el} \cdot \frac{1 + \epsilon_{l/s}^0}{\kappa}\right] - p_t^{el} \tag{A9}$$

Equation (A9) only describes the pressure component of the elastic stress tensor. The total elastic stress σ^{el} results from the following relation:

$$\sigma^{el} = 2G \cdot \mathrm{dev}\left(\varepsilon^{el}\right) - p \cdot \mathbb{I} \tag{A10}$$

In this case, the deviatoric stress $\mathrm{dev}\left(\boldsymbol{\varepsilon}^{\mathrm{el}}\right)$ describes the shape change component of the elastic strain in accordance with Equation (A10). The elastic strain tensor can be written accordingly as follows:

$$\boldsymbol{\varepsilon}^{\mathrm{el}} = \mathrm{dev}\left(\boldsymbol{\varepsilon}^{\mathrm{el}}\right) + \frac{1}{3}\mathrm{trace}\left(\boldsymbol{\varepsilon}^{\mathrm{el}}\right) \cdot \mathbb{I} = \mathrm{dev}\left(\boldsymbol{\varepsilon}^{\mathrm{el}}\right) + \frac{1}{3}\varepsilon_{\mathrm{vol}}^{\mathrm{el}} \cdot \mathbb{I} \tag{A11}$$

The shear modulus G in Equation (A10) can be calculated as a function of the bulk modulus K and Poisson's ratio ν (Equation (A12)). The bulk modulus K in turn is defined as a function of the change in pressure due to an elastic change in volume (Equation (A13)). These relations are taken from [57] and apply to isotropic elastic material behavior. By applying these definitions, the final mechanical model in this work will have isotropic, i.e., direction-independent, mechanical properties:

$$G = \frac{3K(1-2\nu)}{2(1+\nu)} \tag{A12}$$

$$K = -V_{\mathrm{tot}}^{0} \cdot \frac{dp}{dV_{\mathrm{tot}}^{\mathrm{el}}} \tag{A13}$$

Equations (A7) and (A11) give the following definition of $\varepsilon_{\mathrm{vol}}^{\mathrm{el}}$, assuming that stresses and strains only act uniaxial in the 11-direction:

$$\varepsilon_{\mathrm{vol}}^{\mathrm{el}} = \frac{V_{\mathrm{tot}}^{\mathrm{el}}}{V_{\mathrm{tot}}^{0}} - 1 = \varepsilon_{11}^{\mathrm{el}} + \underbrace{\varepsilon_{22}^{\mathrm{el}}}_{=0} + \underbrace{\varepsilon_{33}^{\mathrm{el}}}_{=0} = \varepsilon_{11}^{\mathrm{el}} \tag{A14}$$

Equation (A10) is thus simplified using Equations (A11), (A12) and (A14) as well as the assumptions made here to the following:

$$\sigma_{11}^{\mathrm{el}} = 2\frac{3K(1-2\nu)}{2(1+\nu)} \cdot \left(\varepsilon_{11}^{\mathrm{el}} - \frac{\varepsilon_{11}^{\mathrm{el}} + \cancel{\varepsilon_{22}^{\mathrm{el}}} + \cancel{\varepsilon_{33}^{\mathrm{el}}}}{3}\right) - p = 2K \cdot \varepsilon_{11}^{\mathrm{el}} - p \tag{A15}$$

The strain $\varepsilon_{\mathrm{vol}}^{\mathrm{el}}$ in Equation (A9) can be expressed by the volume ratios using Equation (A7). Substituting this expression of the pressure in Equation (A13) and performing the differentiation, the bulk modulus can be determined as a function of the poroelastic model according to [48,49]:

$$K = -V_{\mathrm{tot}}^{0} \cdot \frac{dp}{dV_{\mathrm{tot}}^{\mathrm{el}}} = \left(p_0 + p_{\mathrm{t}}^{\mathrm{el}}\right) \cdot \exp\left[\left(1 - \frac{V_{\mathrm{tot}}^{\mathrm{el}}}{V_{\mathrm{tot}}^{0}}\right) \cdot \frac{1+\epsilon_{\mathrm{l/s}}^{0}}{\kappa}\right] \cdot \left(\frac{1+\epsilon_{\mathrm{l/s}}^{0}}{\kappa}\right) \tag{A16}$$

Finally, inserting Equation (A16) into Equation (A15) and re-writing the volume fraction as the strain using Equations (A14) and (A7), the uniaxial poroelastic material model used in this work is formed, taking into account that only stresses and strains act in the 11-direction and $\nu = 0$:

$$\sigma_{11}^{\mathrm{el}} = \left(p_0 + p_{\mathrm{t}}^{\mathrm{el}}\right) \cdot \left(2 \cdot \varepsilon_{11}^{\mathrm{el}} \cdot \frac{1+\epsilon_{\mathrm{l/s}}^{0}}{\kappa} - 1\right) \cdot \exp\left[-\varepsilon_{11}^{\mathrm{el}} \cdot \frac{1+\epsilon_{\mathrm{l/s}}^{0}}{\kappa}\right] + p_{\mathrm{t}}^{\mathrm{el}} \tag{A17}$$

Considering that this non-linear stress–strain relationship is intended to be used for compressive scenarios, the strain $\varepsilon_{11}^{\mathrm{el}}$—which acts as an input to this equation—is negated. Lastly, in order to describe the material stress σ rather than the externally applied pressure

p, each pressure is substituted by its respective stress quantity. In the uniaxial case, they are related by a negative sign.

$$\sigma_{11}^{\mathrm{el}} = (\sigma_0 + \sigma_\mathrm{t}) \cdot \left(2 \cdot \varepsilon_{11}^{\mathrm{el}} \cdot \frac{1 + \epsilon_{1/\mathrm{s}}^0}{\kappa} + 1 \right) \cdot \exp\left[\varepsilon_{11}^{\mathrm{el}} \cdot \frac{1 + \epsilon_{1/\mathrm{s}}^0}{\kappa} \right] - \sigma_\mathrm{t} \tag{A18}$$

Appendix C. Fit Results and Error Metrics

Table A1. Fit results and error metrics for the linear-elastic material model for the 10th cycle. The fit results are shown in Figure 9. The first block of columns gives the material, compression rate, and nominal stress as specified by the design of the experiment. The remaining columns give the fitted Young's modulus E along with the coefficient of determination R^2 as well as the maximum and root mean squared errors expressed in relative and absolute terms. Further details regarding the error definition are given in Equation (5) through Equation (10). All values have been rounded to two decimal points.

Specification from Design of Experiment			Linear-Elastic Model — See Figure 3a					
			E MPa	R^2 %	$e_{\mathrm{rel}}^{\mathrm{max}}$ %	$e_{\mathrm{abs}}^{\mathrm{max}}$ MPa	e_{NRMS} %	e_{RMS} MPa
Anode	1C	0.3 MPa	133.04	97.57	21.90	43.75×10^{-3}	8.88	17.73×10^{-3}
		1.0 MPa	432.34	99.21	15.59	31.00×10^{-3}	5.24	10.43×10^{-3}
		3.0 MPa	508.61	96.22	22.10	43.89×10^{-3}	11.55	22.95×10^{-3}
	3C	0.3 MPa	152.22	95.87	28.10	56.17×10^{-3}	11.79	23.56×10^{-3}
		1.0 MPa	413.76	99.35	8.39	16.73×10^{-3}	4.76	9.50×10^{-3}
		3.0 MPa	573.41	98.34	13.51	26.95×10^{-3}	7.71	15.38×10^{-3}
	5C	0.3 MPa	155.46	95.62	28.97	57.87×10^{-3}	12.14	24.25×10^{-3}
		1.0 MPa	386.00	98.82	13.40	26.75×10^{-3}	6.38	12.73×10^{-3}
		3.0 MPa	551.64	97.80	17.80	35.53×10^{-3}	8.77	17.51×10^{-3}
Cathode	1C	0.3 MPa	366.91	98.57	14.07	28.04×10^{-3}	7.10	14.14×10^{-3}
		1.0 MPa	704.94	96.54	18.45	36.66×10^{-3}	11.24	22.33×10^{-3}
		3.0 MPa	971.25	83.17	47.76	94.89×10^{-3}	24.88	49.43×10^{-3}
	3C	0.3 MPa	219.15	92.64	35.71	71.29×10^{-3}	15.93	31.80×10^{-3}
		1.0 MPa	567.26	96.80	18.64	37.19×10^{-3}	10.65	21.26×10^{-3}
		3.0 MPa	1004.64	82.85	59.04	117.61×10^{-3}	24.66	49.13×10^{-3}
	5C	0.3 MPa	212.63	92.00	38.93	77.76×10^{-3}	16.50	32.96×10^{-3}
		1.0 MPa	714.84	93.78	25.48	50.84×10^{-3}	14.91	29.75×10^{-3}
		3.0 MPa	959.43	83.60	48.23	96.20×10^{-3}	24.34	48.55×10^{-3}
Separator	1C	0.3 MPa	46.42	99.36	12.07	24.11×10^{-3}	4.64	9.26×10^{-3}
		1.0 MPa	118.76	99.39	9.95	19.61×10^{-3}	4.61	9.09×10^{-3}
		3.0 MPa	203.30	98.02	16.15	32.01×10^{-3}	8.40	16.65×10^{-3}
	3C	0.3 MPa	44.38	99.05	13.75	27.40×10^{-3}	5.62	11.19×10^{-3}
		1.0 MPa	125.90	99.41	8.10	16.10×10^{-3}	4.50	8.95×10^{-3}
		3.0 MPa	195.66	97.43	25.37	50.59×10^{-3}	9.34	18.63×10^{-3}
	5C	0.3 MPa	42.11	99.44	9.34	18.65×10^{-3}	4.35	8.69×10^{-3}
		1.0 MPa	99.74	99.39	11.79	23.45×10^{-3}	4.55	9.06×10^{-3}
		3.0 MPa	200.20	97.54	21.68	43.20×10^{-3}	9.22	18.38×10^{-3}

Table A2. Fit results and error metrics for the poroelastic material model including translation for the 10th cycle. The fit results are shown in Figure 9. The first block of columns gives the material, compression rate, and nominal stress as specified by the design of the experiment. The remaining columns give the fitted parameters κ and σ_t along with the coefficient of determination R^2 as well as the maximum and root mean squared errors expressed in relative and absolute terms. Further details regarding the error definition are given in Equation (5) through Equation (10). All values have been rounded to two decimal points.

Specification From Design of Experiment			Poroelastic Model — With Translation — See Figure 3a						
			κ	σ_t	R^2	e_{rel}^{max}	e_{abs}^{max}	e_{NRMS}	e_{RMS}
			–	MPa	%	%	MPa	%	MPa
Anode	1C	0.3 MPa	7.28×10^{-3}	0.16	99.90	3.91	7.81×10^{-3}	1.80	3.60×10^{-3}
		1.0 MPa	4.66×10^{-3}	0.39	99.89	6.76	13.44×10^{-3}	1.95	3.88×10^{-3}
		3.0 MPa	1.47×10^{-3}	0.11	99.88	3.99	7.93×10^{-3}	2.06	4.08×10^{-3}
	3C	0.3 MPa	4.45×10^{-3}	0.10	99.98	2.09	4.18×10^{-3}	0.89	1.78×10^{-3}
		1.0 MPa	6.09×10^{-3}	0.50	99.85	5.61	11.19×10^{-3}	2.28	4.55×10^{-3}
		3.0 MPa	2.86×10^{-3}	0.30	99.47	8.81	17.58×10^{-3}	4.35	8.68×10^{-3}
	5C	0.3 MPa	4.19×10^{-3}	0.09	99.95	2.43	4.86×10^{-3}	1.30	2.59×10^{-3}
		1.0 MPa	4.22×10^{-3}	0.30	99.88	4.11	8.20×10^{-3}	2.04	4.07×10^{-3}
		3.0 MPa	2.11×10^{-3}	0.20	99.75	5.52	11.01×10^{-3}	2.97	5.93×10^{-3}
Cathode	1C	0.3 MPa	3.14×10^{-3}	0.24	99.97	2.94	5.86×10^{-3}	1.00	1.99×10^{-3}
		1.0 MPa	1.23×10^{-3}	0.17	99.18	10.22	20.31×10^{-3}	5.48	10.88×10^{-3}
		3.0 MPa	234.66×10^{-6}	0.02	99.80	11.22	22.29×10^{-3}	2.69	5.34×10^{-3}
	3C	0.3 MPa	1.77×10^{-3}	0.05	99.98	1.32	2.64×10^{-3}	0.80	1.60×10^{-3}
		1.0 MPa	1.38×10^{-3}	0.15	99.73	6.01	11.99×10^{-3}	3.10	6.19×10^{-3}
		3.0 MPa	208.07×10^{-6}	0.02	99.49	34.94	69.59×10^{-3}	4.24	8.44×10^{-3}
	5C	0.3 MPa	1.71×10^{-3}	0.05	99.96	4.22	8.44×10^{-3}	1.09	2.18×10^{-3}
		1.0 MPa	716.46×10^{-6}	0.08	99.62	7.47	14.91×10^{-3}	3.67	7.32×10^{-3}
		3.0 MPa	220.99×10^{-6}	0.02	99.85	5.92	11.82×10^{-3}	2.33	4.65×10^{-3}
Separator	1C	0.3 MPa	66.95×10^{-3}	0.42	99.93	3.31	6.61×10^{-3}	1.48	2.96×10^{-3}
		1.0 MPa	25.92×10^{-3}	0.42	99.99	1.36	2.68×10^{-3}	0.60	1.19×10^{-3}
		3.0 MPa	8.34×10^{-3}	0.20	99.89	4.46	8.84×10^{-3}	2.00	3.97×10^{-3}
	3C	0.3 MPa	55.67×10^{-3}	0.32	99.93	3.43	6.84×10^{-3}	1.55	3.09×10^{-3}
		1.0 MPa	25.44×10^{-3}	0.44	99.99	1.81	3.60×10^{-3}	0.64	1.27×10^{-3}
		3.0 MPa	7.04×10^{-3}	0.15	99.90	8.85	17.65×10^{-3}	1.87	3.72×10^{-3}
	5C	0.3 MPa	78.77×10^{-3}	0.46	99.97	2.59	5.17×10^{-3}	1.05	2.11×10^{-3}
		1.0 MPa	31.71×10^{-3}	0.43	99.95	2.62	5.21×10^{-3}	1.24	2.47×10^{-3}
		3.0 MPa	7.24×10^{-3}	0.17	99.92	4.47	8.90×10^{-3}	1.66	3.30×10^{-3}

Table A3. Fit results and error metrics for the poroelastic material model without translation for the 10th cycle. The fit results are shown in Figure 10. The first block of columns gives the material, compression rate, and nominal stress as specified by the design of the experiment. The remaining columns give the fitted parameters κ and σ_t along with the coefficient of determination R^2 as well as the maximum and root mean squared errors expressed in relative and absolute terms. Further details regarding the error definition are given in Equation (5) through Equation (10). All values have been rounded to two decimal points.

Specification from Design of Experiment			Poroelastic Model — No Translation — See Figure 3b							
			κ	σ_t	R^2	e_{rel}^{max}	e_{abs}^{max}	e_{NRMS}	e_{RMS}
			–	MPa	%	%	MPa	%	MPa
Anode	1C	0.3 MPa	3.13×10^{-3}	130.93×10^{-6}	99.51	7.22	21.54×10^{-3}	2.67	7.95×10^{-3}
		1.0 MPa	3.56×10^{-3}	380.51×10^{-6}	99.92	1.32	12.97×10^{-3}	0.35	3.41×10^{-3}
		3.0 MPa	8.29×10^{-3}	480.39×10^{-6}	98.75	1.13	33.42×10^{-3}	0.45	13.18×10^{-3}
	3C	0.3 MPa	2.78×10^{-3}	1.61×10^{-3}	99.88	3.92	11.69×10^{-3}	1.34	3.98×10^{-3}
		1.0 MPa	3.74×10^{-3}	299.49×10^{-6}	99.85	1.51	14.85×10^{-3}	0.47	4.64×10^{-3}
		3.0 MPa	7.87×10^{-3}	1.96×10^{-3}	99.80	0.83	24.51×10^{-3}	0.18	5.28×10^{-3}
	5C	0.3 MPa	2.50×10^{-3}	206.21×10^{-6}	99.88	4.03	12.02×10^{-3}	1.37	4.08×10^{-3}
		1.0 MPa	4.06×10^{-3}	1.73×10^{-3}	99.96	0.89	8.75×10^{-3}	0.23	2.30×10^{-3}
		3.0 MPa	8.25×10^{-3}	4.70×10^{-3}	99.71	0.95	28.11×10^{-3}	0.22	6.38×10^{-3}
Cathode	1C	0.3 MPa	981.35×10^{-6}	6.33×10^{-6}	98.79	9.38	27.97×10^{-3}	4.36	12.99×10^{-3}
		1.0 MPa	1.62×10^{-3}	42.64×10^{-6}	99.63	2.59	25.42×10^{-3}	0.74	7.30×10^{-3}
		3.0 MPa	2.83×10^{-3}	66.88×10^{-6}	94.26	3.36	99.04×10^{-3}	0.98	28.87×10^{-3}
	3C	0.3 MPa	1.37×10^{-3}	223.44×10^{-6}	99.99	0.80	2.39×10^{-3}	0.42	1.26×10^{-3}
		1.0 MPa	2.09×10^{-3}	306.36×10^{-6}	99.86	2.46	24.23×10^{-3}	0.46	4.51×10^{-3}
		3.0 MPa	2.75×10^{-3}	26.10×10^{-6}	93.08	3.17	93.39×10^{-3}	1.06	31.20×10^{-3}
	5C	0.3 MPa	1.32×10^{-3}	22.68×10^{-6}	99.97	2.80	8.35×10^{-3}	0.68	2.01×10^{-3}
		1.0 MPa	1.48×10^{-3}	40.69×10^{-6}	99.45	4.16	40.91×10^{-3}	0.90	8.87×10^{-3}
		3.0 MPa	2.99×10^{-3}	111.06×10^{-6}	92.99	2.89	85.31×10^{-3}	1.08	31.75×10^{-3}
Separator	1C	0.3 MPa	13.97×10^{-3}	12.79×10^{-6}	98.89	11.57	34.51×10^{-3}	4.09	12.20×10^{-3}
		1.0 MPa	17.60×10^{-3}	825.17×10^{-9}	99.99	0.27	2.69×10^{-3}	0.12	1.18×10^{-3}
		3.0 MPa	28.95×10^{-3}	1.20×10^{-6}	99.71	0.88	25.83×10^{-3}	0.22	6.35×10^{-3}
	3C	0.3 MPa	13.75×10^{-3}	194.35×10^{-9}	99.10	10.77	32.08×10^{-3}	3.66	10.90×10^{-3}
		1.0 MPa	16.48×10^{-3}	260.73×10^{-9}	99.99	0.41	4.08×10^{-3}	0.13	1.29×10^{-3}
		3.0 MPa	30.54×10^{-3}	25.90×10^{-6}	99.31	1.16	34.31×10^{-3}	0.33	9.68×10^{-3}
	5C	0.3 MPa	15.87×10^{-3}	51.98×10^{-6}	98.75	11.81	35.20×10^{-3}	4.34	12.94×10^{-3}
		1.0 MPa	21.08×10^{-3}	845.19×10^{-9}	99.96	0.61	6.00×10^{-3}	0.23	2.25×10^{-3}
		3.0 MPa	28.97×10^{-3}	838.04×10^{-9}	99.54	0.96	28.37×10^{-3}	0.27	7.96×10^{-3}

References

1. Sauerteig, D.; Hanselmann, N.; Arzberger, A.; Reinshagen, H.; Ivanov, S.; Bund, A. Electrochemical-mechanical coupled modeling and parameterization of swelling and ionic transport in lithium-ion batteries. *J. Power Sources* **2018**, *378*, 235–247. [CrossRef]
2. Müller, V. Investigation of the Influence of Mechanical Pressure on the Aging and the Expansion of Silicon-Containing Lithium-Ion Batteries. Ph.D. Thesis, University of Bayreuth, Bayreuth, Germany, 2020. [CrossRef]
3. Spingler, F.B.; Friedrich, S.; Kücher, S.; Schmid, S.; López-Cruz, D.; Jossen, A. The Effects of Non-Uniform Mechanical Compression of Lithium-Ion Cells on Local Current Densities and Lithium Plating. *J. Electrochem. Soc.* **2021**, *168*, 110515. [CrossRef]
4. Spielbauer, M.; Peteler, F.; Németh, A.; Soellner, J.; Berg, P.; Bohlen, O.; Jossen, A. An analysis of the current state and obstacles in discrete layered finite element simulation of crushing cylindrical lithium-ion cells. *J. Energy Storage* **2023**, *72*, 108029. [CrossRef]
5. Kalnaus, S.; Wang, Y.; Li, J.; Kumar, A.; Turner, J.A. Temperature and strain rate dependent behavior of polymer separator for Li-ion batteries. *Extrem. Mech. Lett.* **2018**, *20*, 73–80. [CrossRef]
6. Ding, L.; Zhang, C.; Wu, T.; Yang, F.; Lan, F.; Cao, Y.; Xiang, M. Effect of temperature on compression behavior of polypropylene separator used for Lithium-ion battery. *J. Power Sources* **2020**, *466*, 228300. [CrossRef]
7. Ding, L.; Li, D.; Du, F.; Zhang, D.; Zhang, S.; Xu, R.; Wu, T. Mechanical behaviors and ion transport variation of lithium-ion battery separators under various compression conditions. *J. Power Sources* **2022**, *543*, 231838. [CrossRef]
8. Wang, Y.; Xing, Y.; Li, Q.M. A Hyper-Viscoelastic Model for Battery Separators Based on Inverse-Stress-Solution Parametrical Calibration Method. *Int. J. Mech. Sci.* **2022**, *225*, 107361. [CrossRef]

9. Aufschläger, A.; Kücher, S.; Kraft, L.; Spingler, F.; Niehoff, P.; Jossen, A. High precision measurement of reversible swelling and electrochemical performance of flexibly compressed 5 Ah NMC622/graphite lithium-ion pouch cells. *J. Energy Storage* **2023**, *59*, 106483. [CrossRef]
10. von Kessel, O.; Hoehl, T.; Heugel, P.; Brauchle, F.; Vrankovic, D.; Birke, K.P. Electrochemical-Mechanical Parameterization and Modeling of Expansion, Pressure, and Porosity Evolution in NMC811|SiOx-Graphite Lithium-Ion Cells. *J. Electrochem. Soc.* **2023**, *170*, 090534. [CrossRef]
11. Schabenberger, T.; Kücher, S.; Aufschläger, A.; Jossen, A. Impact of applied and preceding pressure on performance and reversible swelling of lithium-ion pouch cells with varying microporous separators. *J. Energy Storage* **2024**, *102*, 113910. [CrossRef]
12. Rieger, B.; Erhard, S.V.; Rumpf, K.; Jossen, A. A New Method to Model the Thickness Change of a Commercial Pouch Cell during Discharge. *J. Electrochem. Soc.* **2016**, *163*, A1566–A1575. [CrossRef]
13. Zhou, W. Effects of external mechanical loading on stress generation during lithiation in Li-ion battery electrodes. *Electrochim. Acta* **2015**, *185*, 28–33. [CrossRef]
14. Liu, X.M.; Arnold, C.B. Effects of Cycling Ranges on Stress and Capacity Fade in Lithium-Ion Pouch Cells. *J. Electrochem. Soc.* **2016**, *163*, A2501–A2507. [CrossRef]
15. Cannarella, J.; Arnold, C.B. Stress evolution and capacity fade in constrained lithium-ion pouch cells. *J. Power Sources* **2014**, *245*, 745–751. [CrossRef]
16. Cannarella, J.; Arnold, C.B. State of health and charge measurements in lithium-ion batteries using mechanical stress. *J. Power Sources* **2014**, *269*, 7–14. [CrossRef]
17. Bucci, G.; Swamy, T.; Bishop, S.; Sheldon, B.W.; Chiang, Y.M.; Carter, W.C. The Effect of Stress on Battery-Electrode Capacity. *J. Electrochem. Soc.* **2017**, *164*, A645–A654. [CrossRef]
18. Duan, J.; Tang, X.; Dai, H.; Yang, Y.; Wu, W.; Wei, X.; Huang, Y. Building Safe Lithium-Ion Batteries for Electric Vehicles: A Review. *Electrochem. Energy Rev.* **2020**, *3*, 1–42. [CrossRef]
19. Kebede, A.A.; Kalogiannis, T.; van Mierlo, J.; Berecibar, M. A comprehensive review of stationary energy storage devices for large scale renewable energy sources grid integration. *Renew. Sustain. Energy Rev.* **2022**, *159*, 112213. [CrossRef]
20. Rey, S.O.; Romero, J.A.; Romero, L.T.; Martínez, À.F.; Roger, X.S.; Qamar, M.A.; Domínguez-García, J.L.; Gevorkov, L. Powering the Future: A Comprehensive Review of Battery Energy Storage Systems. *Energies* **2023**, *16*, 6344. [CrossRef]
21. Kotter, P.; Kisters, T.; Schleicher, A. Dynamic impact tests to characterize the crashworthiness of large-format lithium-ion cells. *J. Energy Storage* **2019**, *26*, 100948. [CrossRef]
22. M. Braun Inertgas-Systeme GmbH. Unilab Pro: Inert Gas Glovebox Workstation. 2024. Available online: https://www.mbraun.com/de/produkte/glovebox-workstations.html (accessed on 5 May 2024).
23. Nogamigiken Co., Ltd.. *Handheld Electrode Punch*; Nogamigiken Co., Ltd.: Hitachiomiya, Japan, 2024.
24. ZwickRoell GmbH & Co. KG. *Produktinformation: Material-Prüfmaschinen AllroundLine Z005 bis Z100*; ZwickRoell GmbH & Co. KG: Ulm, Germany, 2024.
25. ZwickRoell GmbH & Co. KG. *Produktinformation: Kraftaufnehmer Xforce P, Xforce HP und Xforce K*; ZwickRoell GmbH & Co. KG: Ulm, Germany, 2024.
26. Berthold, R.; Eichinger, A.; Ermlich, W.; Fiek, G.; Föppl, L.; Glocker, R.; Lehr, E.; Vaupel, O.; Siebel, E. *Prüf- und Meßeinrichtungen*; Springer: Berlin/Heidelberg, Germany, 1940. [CrossRef]
27. Subaric-Leitis, A.; Seiffert, B.; Ullner, C. Ergebnisunsicherheit ermitteln: Konformitätsprüfung einachsiger Zug-/Druckprüfmaschinen. *Mater. Test.* **2000**, *42*, 114–117. [CrossRef]
28. Findeisen, D. Grundlegendes zur Steifigkeit von Werkstoffprüfmaschinen. *Mater. Test.* **2017**, *59*, 379–385. [CrossRef]
29. Müller, V.; Scurtu, R.G.; Memm, M.; Danzer, M.A.; Wohlfahrt-Mehrens, M. Study of the influence of mechanical pressure on the performance and aging of Lithium-ion battery cells. *J. Power Sources* **2019**, *440*, 227148. [CrossRef]
30. Li, Y.; Wei, C.; Sheng, Y.; Jiao, F.; Wu, K. Swelling Force in Lithium-Ion Power Batteries. *Ind. Eng. Chem. Res.* **2020**, *59*, 12313–12318. [CrossRef]
31. Hahn, S.; Theil, S.; Kroggel, J.; Birke, K.P. Pressure Prediction Modeling and Validation for Lithium-Ion Pouch Cells in Buffered Module Assemblies. *J. Energy Storage* **2021**, *40*, 102517. [CrossRef]
32. Daubinger, P.; Schelter, M.; Petersohn, R.; Nagler, F.; Hartmann, S.; Herrmann, M.; Giffin, G.A. Impact of Bracing on Large Format Prismatic Lithium–Ion Battery Cells during Aging. *Adv. Energy Mater.* **2021**, *12*, 2102448. [CrossRef]
33. Aufschläger, A.; Durdel, A.; Kraft, L.; Jossen, A. Optimizing mechanical compression for cycle life and irreversible swelling of high energy and high power lithium-ion pouch cells. *J. Energy Storage* **2024**, *76*, 109883. [CrossRef]
34. Petursdottir, E.; Kohlhuber, M.; Ehrenberg, H. Influence from Mechanical Stress on State of Health of Large Prismatic Lithium-Ion-Cells under Various Temperatures. *J. Electrochem. Soc.* **2024**, *171*, 070510. [CrossRef]
35. Thompson. *Ansys Mechanical Apdl for Finite Element Analysis*; Elsevier Science & Technology: Amsterdam, The Netherlands, 2017.
36. Kermani, G.; Sahraei, E. Review: Characterization and Modeling of the Mechanical Properties of Lithium-Ion Batteries. *Energies* **2017**, *10*, 1730. [CrossRef]
37. Seulin, M.; Michel, C.; Lapoujade, V.; L'Eplattenier, P. Mechanical modeling Li-Ion cell crush experiments using LS-DYNA. In Proceedings of the 11th European LS-DYNA Conference 2017: Salzburg, Augstria, 9–11 May 2017. Available online: https://lsdyna.ansys.com/wp-content/uploads/attachments/mechanical-modeling-of-li-ion-cell-crush-experiments-using-ls-dyna.pdf (accessed on 2 July 2024).

38. Sahraei, E.; Keshavarzi, M.M.; Zhang, X.; Lai, B. Mechanical Properties of Prismatic Li-Ion Batteries—Electrodes, Cells, and Stacks. *J. Electrochem. Energy Convers. Storage* **2022**, *19*, 041008 . [CrossRef]
39. Zou, Z.; Xu, F.; Tian, H.; Niu, X. Testing and impact modeling of lithium-ion prismatic battery under quasi-static and dynamic mechanical abuse. *J. Energy Storage* **2023**, *68*, 107639. [CrossRef]
40. Hooke, R.; Yonge, J. *Lectures and Collections*; Martin, John: London, UK, 1678.
41. Meille, S.; Garboczi, E.J. Linear elastic properties of 2D and 3D models of porous materials made from elongated objects. *Model. Simul. Mater. Sci. Eng.* **2001**, *9*, 371–390. [CrossRef]
42. Grazioli, D.; Zadin, V.; Brandell, D.; Simone, A. Electrochemical-mechanical modeling of solid polymer electrolytes: Stress development and non-uniform electric current density in trench geometry microbatteries. *Electrochim. Acta* **2019**, *296*, 1142–1162. [CrossRef]
43. Wang, B.; Réthoré, J.; Aifantis, K.E. Capturing the stress evolution in electrode materials that undergo phase transformations during electrochemical cycling. *Int. J. Solids Struct.* **2021**, *224*, 111032. [CrossRef]
44. Ballay, F.; Braun, A.; Hein, S.; Hellmuth, M.; Krieg, M.; Kuhn, V.; Lindau, D.; Nutsch, W.; Stemmler, C.; Traub, M.; et al. *Fachkunde für Maurer/Maurerinnen, Beton- und Stahlbetonbauer/Beton- und Stahlbetonbauerinnen, Zimmerer/Zimmerinnen und Bauzeichner/Bauzeichnerinnen: Fachkunde Bau für Maurer/Maurerinnen, Beton- und Stahlbetonbauer/Beton- und Stahlbetonbauerinnen, Zimmerer/Zimmerinnen und Bauzeichner/Bauzeichnerinnen*, 18., überarbeitete auflage ed.; Europa-Fachbuchreihe für Bautechnik, Verlag Europa-Lehrmittel, Nourney, Vollmer GmbH & Co. KG: Haan-Gruiten, Germany, 2020.
45. Rouquerol, J.; Baron, G.; Denoyel, R.; Giesche, H.; Groen, J.; Klobes, P.; Levitz, P.; Neimark, A.V.; Rigby, S.; Skudas, R.; et al. Liquid intrusion and alternative methods for the characterization of macroporous materials (IUPAC Technical Report). *Pure Appl. Chem.* **2011**, *84*, 107–136. [CrossRef]
46. Athy, L.F. Density, Porosity and Compaction of Sedimentary Rocks. *AAPG Bull.* **1930**, *14*, 1–24.
47. Weiss, J.L.; König, L.F. *Groundwater: Modelling, Management and Contamination*; Nova Science Publishers Incorporated: Hauppauge, NY, USA, 2009.
48. Li, C.; Borja, R.I. *Finite Element Formulation of Poro-Elasticity Suitable for Large Deformation Dynamic Analysis*; John A. Blume Earthquake Engineering Center Technical Report Series; Stanford University Press: Redwood City, CA, USA, 2005; Volume 147.
49. Dassault Systèmes. Abaqus 6.11: Analysis User's Manual: Volume IV: Materials. 2011. Available online: http://abaqusdocs.eait.uq.edu.au/v6.11/pdf_books/ANALYSIS_4.pdf (accessed on 1 July 2024).
50. Scales, M.; Kornuta, J.A.; Switzner, N.; Veloo, P. Automated Calculation of Strain Hardening Parameters from Tensile Stress vs. Strain Data for Low Carbon Steel Exhibiting Yield Point Elongation. *Exp. Tech.* **2023**, *47*, 1311–1322. [CrossRef]
51. Maaß, R.; van Petegem, S.; Ma, D.; Zimmermann, J.; Grolimund, D.; Roters, F.; van Swygenhoven, H.; Raabe, D. Smaller is stronger: The effect of strain hardening. *Acta Mater.* **2009**, *57*, 5996–6005. [CrossRef]
52. Rajaram, G.; Kumaran, S.; Suwas, S. Effect of strain rate on tensile and compression behaviour of Al–Si/graphite composite. *Mater. Sci. Eng. A* **2011**, *528*, 6271–6278. [CrossRef]
53. Wen, J.; Wei, Y.; Cheng, Y.T. Stress evolution in elastic-plastic electrodes during electrochemical processes: A numerical method and its applications. *J. Mech. Phys. Solids* **2018**, *116*, 403–415. [CrossRef]
54. Shpigel, N.; Lukatskaya, M.R.; Sigalov, S.; Ren, C.E.; Nayak, P.; Levi, M.D.; Daikhin, L.; Aurbach, D.; Gogotsi, Y. In Situ Monitoring of Gravimetric and Viscoelastic Changes in 2D Intercalation Electrodes. *ACS Energy Lett.* **2017**, *2*, 1407–1415. [CrossRef]
55. Dargel, V.; Jäckel, N.; Shpigel, N.; Sigalov, S.; Levi, M.D.; Daikhin, L.; Presser, V.; Aurbach, D. In Situ Multilength-Scale Tracking of Dimensional and Viscoelastic Changes in Composite Battery Electrodes. *ACS Appl. Mater. Interfaces* **2017**, *9*, 27664–27675. [CrossRef] [PubMed]
56. Sauerteig, D. Implementierung und Parametrierung eines Physikalischen Simulationsmodells einer Lithium-Ionen Zelle zur Analyse Elektrochemisch-Mechanischer Wechselwirkungen. Ph.D. Thesis, Technische Universität Ilmenau, Ilmenau, Germany, 1 November 2018.
57. Dvorkin, J. *Rock Physics Handbook—Tools for Seismic Analysis of Porous Media*; Cambridge University Press: Cambridge, MA, USA, 2009. [CrossRef]

Disclaimer/Publisher's Note: The statements, opinions and data contained in all publications are solely those of the individual author(s) and contributor(s) and not of MDPI and/or the editor(s). MDPI and/or the editor(s) disclaim responsibility for any injury to people or property resulting from any ideas, methods, instructions or products referred to in the content.